A Numerical Rocks Physics Approach to Model Wave Propagation in Hydrocarbon Reservoirs

2017 PIMS WORKSHOP on Imaging and Inversion, Calgary University, Calgary, Alberta, May 23-26, 2017

Juan E. Santos,

Department of Mathematics, Purdue University, West Lafayette, Indiana, USA, Instituto del Gas y del Petróleo (IGPUBA), Universidad de Buenos Aires (UBA), Argentina, and Universidad Nacional de La Plata (UNLP), Argentina.

In collaboration with P. M. Gauzellino (UNLP), G. B. Savioli (UBA), A. Sanchez Camus (UNLP) and R. Martinez Corredor, (UNLP).

March 30, 2017

Seismic waves in fluid-saturated poroelastic materials. I

- Fast compressional or shear waves travelling through a fluid-saturated porous material (a Biot medium) containing heterogeneities on the order of centimeters (mesoscopic scale) suffer attenuation and dispersion observed in seismic data.
- The mesoscopic loss effect occurs because different regions of the medium may undergo different strains and fluid pressures.
- This in turn induces fluid flow and Biot slow waves causing energy losses and velocity dispersion due to energy transfer between wave modes.

Seismic waves in fluid-saturated poroelastic materials. II

- Since extremely fine meshes are needed to represent these type of mesoscopic-scale heterogeneities, numerical simulations are very expensive or not feasible.
- Alternative: In the context of Numerical Rock Physics, perform compressibility and shear time-harmonic experiments to determine a long-wave equivalent viscoelastic medium to a highly heterogeneous Biot medium.
- This viscoelastic medium has in the average the same attenuation and velocity dispersion than the highly heterogeneous Biot medium.
- Each experiment is associated with a Boundary Value Problem (BVP) that is solved using the Finite Element Method (FEM).

Biot's equations in the diffusive range of frequencies.

Frequency-domain stress-strain relations in a Biot medium

$$\tau_{kl}(\mathbf{u}) = 2\mu\,\epsilon_{kl}(\mathbf{u}^s) + \delta_{kl}\left(\lambda_u\,\nabla\cdot\mathbf{u}^s + B\nabla\cdot\mathbf{u}^f\right),$$
$$p_f(\mathbf{u}) = -B\nabla\cdot\mathbf{u}^s - M\nabla\cdot\mathbf{u}^f,$$

$\mathbf{u} = (\mathbf{u}^s, \mathbf{u}^f)$, $\mathbf{u}^s = (u_1^s, u_3^s), \mathbf{u}^f = (u_1^f, u_3^f)$.

Biot's equations in the diffusive range:

$$\nabla\cdot\tau(\mathbf{u}) = 0,$$
$$\mathrm{i}\omega\eta\kappa^{-1}\mathbf{u}^f + \nabla p_f(\mathbf{u}) = 0,$$

η: fluid viscosity, κ:frame permeability.

The complex P-wave modulus of the long-wave equivalent viscoelastic medium. I

Biots' s equations are be solved in the 2-D case on square sample $\Omega = (0, L)^2$ with boundary $\Gamma = \Gamma^L \cup \Gamma^B \cup \Gamma^R \cup \Gamma^T$ in the (x_1, x_3)-plane. The domain Ω is a representative sample of our fluid saturated poroelastic material.

$$\Gamma^L = \{(x_1, x_3) \in \Gamma : x_1 = 0\}, \quad \Gamma^R = \{(x_1, x_3) \in \Gamma : x_1 = L\},$$
$$\Gamma^B = \{(x_1, x_3) \in \Gamma : x_3 = 0\}, \quad \Gamma^T = \{(x_1, x_3) \in \Gamma : x_3 = L\}.$$

For determining the complex plane wave modulus, we solve Biots' s equations with the boundary conditions

$$\tau(\mathbf{u})\nu \cdot \nu = -\Delta P, \quad (x_1, x_3) \in \Gamma^T,$$
$$\tau(\mathbf{u})\nu \cdot \chi = 0, \quad (x_1, x_3) \in \Gamma,$$
$$\mathbf{u}^s \cdot \nu = 0, \quad (x_1, x_3) \in \Gamma^L \cup \Gamma^R \cup \Gamma^B,$$
$$\mathbf{u}^f \cdot \nu = 0, \quad (x_1, x_3) \in \Gamma.$$

The complex P-wave modulus of the long-wave equivalent viscoelastic medium. II

The *equivalent* undrained complex plane-wave modulus $\overline{E_u}(\omega)$ is determined by the relation

$$\frac{\Delta V(\omega)}{V} = -\frac{\Delta P}{\overline{E_u}(\omega)},$$

valid for a viscoelastic homogeneous medium in the quasi-static case. V: original volume of the sample. Then to approximate $\Delta V(\omega)$ use

$$\Delta V(\omega) \approx L u_3^{s,T}(\omega),$$

$u_3^{s,T}(\omega)$: average vertical solid displacements $u_3^s(x_1, L, \omega)$ on Γ^T.

The complex shear modulus of the long-wave equivalent viscoelastic medium. I

Solve Biots' s equations with the boundary conditions

$$-\tau(\mathbf{u})\nu = \mathbf{g}, \quad (x_1, x_3) \in \Gamma^T \cup \Gamma^L \cup \Gamma^R,$$
$$\mathbf{u}^s = 0, \quad (x, y) \in \Gamma^B,$$
$$\mathbf{u}^f \cdot \nu = 0, \quad (x, y) \in \Gamma,$$

$$\mathbf{g} = \begin{cases} (0, \Delta G), & (x_1, x_3) \in \Gamma^L, \\ (0, -\Delta G), & (x_1, x_3) \in \Gamma^R, \\ (-\Delta G, 0), & (x_1, x_3) \in \Gamma^T. \end{cases}$$

The change in shape of the rock sample allows to recover its *equivalent* complex shear modulus $\overline{\mu}_c(\omega)$ using the relation

$$\mathrm{tg}(\theta(\omega)) = \frac{\Delta T}{\overline{\mu}_c(\omega)},$$

$\theta(\omega)$: departure angle from the original positions of the lateral boundaries

The complex shear modulus of the long-wave equivalent viscoelastic medium. II

To find an approximation to $\mathrm{tg}(\theta(\omega))$, compute the average horizontal displacement $u_1^{s,T}(\omega)$ of the horizontal displacements $u_1^s(x_1, L, \omega)$ at the top boundary Γ^T. Then use

$$\mathrm{tg}(\theta(\omega)) \approx u_1^{s,T}(\omega)/L,$$

that allows to determine the shear modulus $\overline{\mu}_c(\omega)$

Phase velocities and Quality factors.

The complex P-wave and shear velocities are

$$v_{sc}(\omega) = \sqrt{\frac{\overline{\mu}_c(\omega)}{\overline{\rho}}} \quad v_{pc}(\omega) = \sqrt{\frac{\overline{E_u}(\omega)}{\overline{\rho}}},$$

The compressional phase velocities $v_p(\omega), v_s(\omega)$ and quality factor $Q_p(\omega), Q_s(\omega)$ are

$$v_p(\omega) = \left[\mathrm{Re}\left(\frac{1}{v_{pc}(\omega)}\right)\right]^{-1}, \quad \frac{1}{Q_p(\omega)} = \frac{\mathrm{Im}(v_{pc}(\omega)^2)}{\mathrm{Re}(v_{pc}(\omega)^2)}.$$

$$v_s(\omega) = \left[\mathrm{Re}\left(\frac{1}{v_{sc}(\omega)}\right)\right]^{-1}, \quad \frac{1}{Q_s(\omega)} = \frac{\mathrm{Im}(v_{sc}(\omega)^2)}{\mathrm{Re}(v_{sc}(\omega)^2)}.$$

Schematic representation of the experiments to determine the complex P-wave and shear modulus

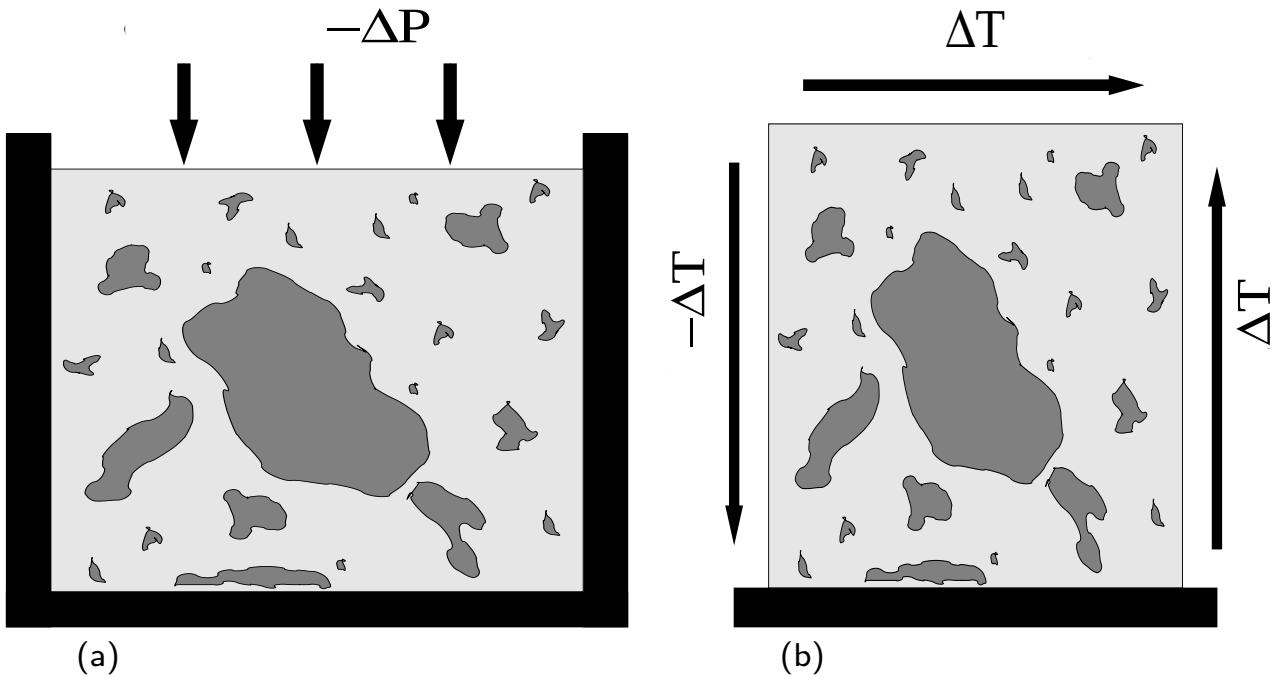

Figures (a) show how to determine $E_u(\omega)$, (b) show how to determine $\mu_c(\omega)$.

Variational formulation of the BVP's. I

$$H^{1,P}(\Omega) = \{\mathbf{v} \in [H^1(\Omega)]^2 : \mathbf{v}\cdot\nu = 0 \ \text{ on } \Gamma^L \cup \Gamma^R \cup \Gamma^B\},$$

$$H^{1,T}_{0,B}(\Omega) = \{\mathbf{v} \in [H^1(\Omega)]^2 : \mathbf{v} = 0 \ \text{ on } \Gamma^B\},$$

$$H_0(\mathrm{div},\Omega) = \{\mathbf{v} \in [L^2(\Omega)]^2 : \ \nabla\cdot\mathbf{v} \in L^2(\Omega), \mathbf{v}\cdot\nu = 0 \ \text{ on } \Gamma\}.$$

$$\mathcal{V}^{(P)} = \left[H^{1,P}(\Omega)\right]^2 \times H_0(\mathrm{div};\Omega), \mathcal{V}^{(T)} = \left[H^{1,T}_{0,B}(\Omega)\right]^2 \times H_0(\mathrm{div};\Omega).$$

Let

$$\Lambda(\mathbf{u},\mathbf{v}) = \mathrm{i}\omega\left(\eta\,\kappa^{-1}\mathbf{u}^f, \mathbf{v}^f\right) + \sum_{l,m}\left(\tau_{lm}(\mathbf{u}), \varepsilon_{lm}(\mathbf{v}^s)\right)$$

$$-\left(p_f(\mathbf{u}), \nabla\cdot\mathbf{v}^f\right)\Big)$$

Variational formulation of the BVP's. II

To determine $E_u(\omega)$: find $u^{(P)} = (u^{(s,P)}, u^{(f,P)}) \in \mathcal{V}^{(P)}$ such that

$$\Lambda(\mathbf{u}^{(P)}, \mathbf{v}) = -\langle \Delta P, \mathbf{v}^s \cdot \nu \rangle_{\Gamma^T}, \quad \forall \quad \mathbf{v} = \left(\mathbf{v}^s, \mathbf{v}^f\right) \in \mathcal{V}^{(P)}.$$

To determine $\mu_c(\omega)$: find $\mathbf{u}^{(T)} = (\mathbf{u}^{(s,T)}, \mathbf{u}^{(f,T)}) \in \mathcal{V}^{(T)}$ such that

$$\Lambda(\mathbf{u}^{(T)}, \mathbf{v}) = -\langle \mathbf{g}, \mathbf{v}^s \rangle_{\Gamma \setminus \Gamma^B}, \qquad \forall \quad \mathbf{v} = \left(\mathbf{v}^s, \mathbf{v}^f\right) \in \mathcal{V}^{(S)}.$$

Finite element procedures. I

$$\mathcal{N}^{h,P} = \{\mathbf{v} : \mathbf{v}|_{R^j} \in [P_{1,1}(R^j)]^2, \mathbf{v}\cdot\nu = 0 \text{ on } \Gamma^L \cup \Gamma^R \cup \Gamma^B\}$$
$$\mathcal{N}^{h,T}_{0,B} = \{\mathbf{v} : \mathbf{v}|_{R^j} \in [P_{1,1}(R^j)]^2, \mathbf{v} = 0 \text{ on } \Gamma^B\} \cap [C^0(\overline{\Omega})]^2.$$
$$\mathcal{V}^h_0 = \{\mathbf{v} : \mathbf{v}|_{R^j} \in P_{1,0} \times P_{0,1}, \mathbf{v}\cdot\nu = 0 \text{ on } \Gamma\}.$$
$$\mathcal{V}^{(h,P)} = \mathcal{N}^{h,P} \times \mathcal{V}^h_0, \quad \mathcal{V}^{(h,T)} = \mathcal{N}^{h,T}_{0,B} \times \mathcal{V}^h_0.$$

The FE procedures to determine $E_u(\omega)$ and $\mu_c(\omega)$:

$$\Lambda(\mathbf{u}^{(h,P)}, \mathbf{v}) = -\langle \Delta P, \mathbf{v}^s \cdot \nu\rangle_{\Gamma^T}, \forall \quad \mathbf{v} = \left(\mathbf{v}^s, \mathbf{v}^f\right) \in \mathcal{V}^{(h,P)},$$
$$\Lambda(\mathbf{u}^{(h,T)}, \mathbf{v}) = -\langle \mathbf{g}, \mathbf{v}^s\rangle_{\Gamma\setminus\Gamma^B}, \quad \forall \mathbf{v} = \left(\mathbf{v}^s, \mathbf{v}^f\right) \in \mathcal{V}^{(h,T)}.$$

Finite element procedures. II

The mesh size h, it has to be small enough so that diffusion process associated with the fluid pressure equilibration is accurately resolved.
The diffusion length is given by the relation length

$$L_d = \sqrt{\frac{2\pi\kappa K_f}{\eta\omega}},$$

We take h so that the minimum diffusion length is discretized with at least 3 mesh points at the highest frequency, which is sufficient to represent a (smooth) diffusion-type process.
Besides, the size of the rock sample is not arbitrary: it has to be big enough to constitute a representative part of the Biot medium but, at the same time, it has to be much smaller than the wavelengths associated with each frequency.

Application to patchy gas-brine saturation

Patchy gas-brine saturation arises in hydrocarbon reservoirs, where regions of non-uniform patchy saturation occur at gas-brine contacts. Patchy-saturation patterns produce very important mesoscopic loss effects at the seismic band of frequencies, as was first shown by J. E. White (GPY, 1975).

To study these effects, consider porous samples with spatially variable gas-brine distribution in the form of irregular patches fully saturated with gas and zones fully saturated with brine. The domain Ω is a square of side length 50 cm, and a 75×75 mesh uniform is used.

The frequency is varied from 0 to 500 Hz and the solid matrix is sandstone 1 with properties given in Table 1. The fluids porperties are given in Table 2.

Material properties of the solid frames used in the experiments.

Table: Physical properties of the solid materials

	Sandstone 1	**Sandstone 2**	**Shale**
K_s	37 GPa	37 GPa	25 GPa
ρ_s	2650 $\mathrm{kg/m^3}$	2650 $\mathrm{kg/m^3}$	2650 $\mathrm{kg/m^3}$
ϕ	0.3	0.2	0.3
K_m	4.8 GPa	12.1 GPa	3.3 GPa
μ_m	5.7 GPa	14.4 GPa	1.2 GPa
κ	$10^{-12}\,\mathrm{m^2}$	$0.23 \times 10^{-12}\,\mathrm{m^2}$	$1.5 \times 10^{-17}\mathrm{m^2}$

Properties of the fluids used in the experiments.

Table: Physical properties of the fluids

	Brine	**Gas**
K_f	2.25 GPa	0.012 GPa
ρ_f	1040 $\mathrm{kg/m^3}$	78 $\mathrm{kg/m^3}$
η	0.003 Pa $\cdot$ s	0.00015 Pa $\cdot$ s

Patchy gas-brine distribution for two different correlation lengths

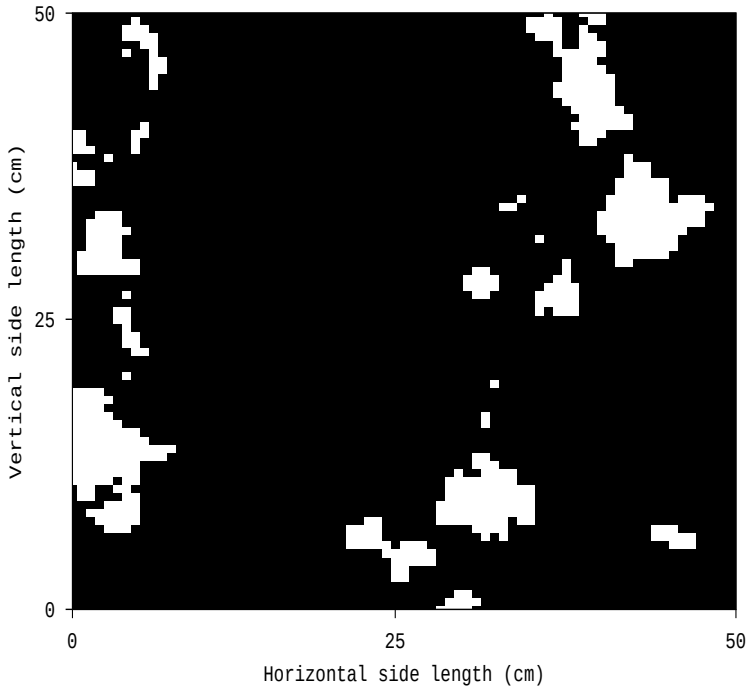

(a)

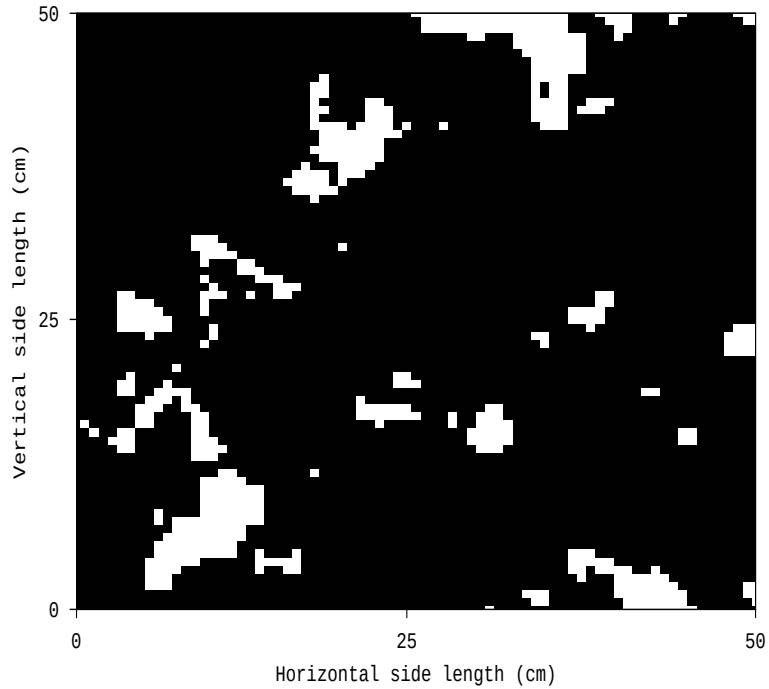

(b)

(a): correlation length 10 cm (b): correlation lengths 5 cm.

Compressional phase velocity and inverse quality factors for two different correlation lengths

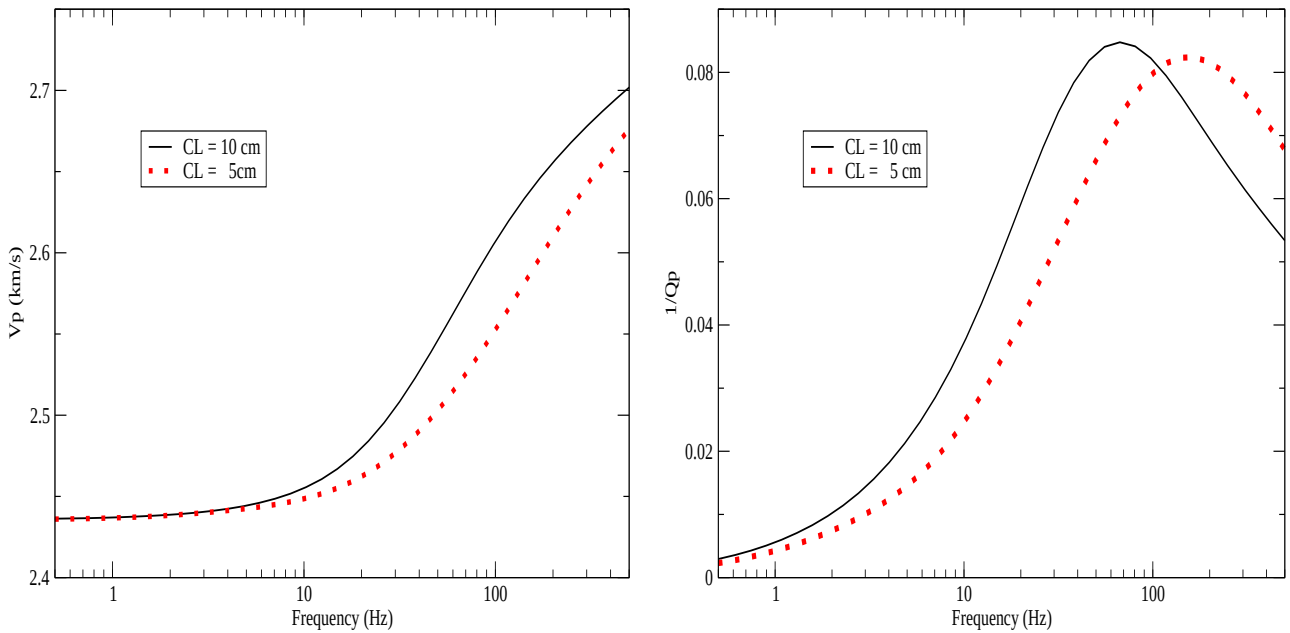

(a) (b)

(a): Compressional phase velocity (b): Inverse quality factors.

Pressure distribution (Pa) at two different frequencies.

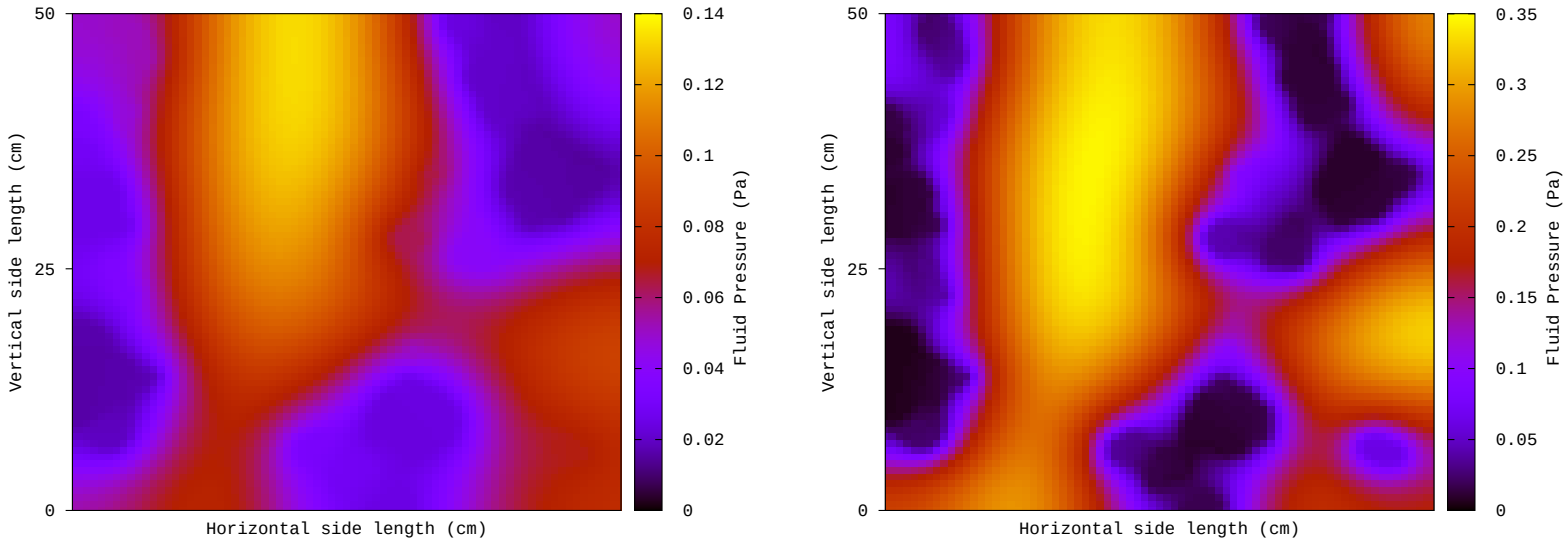

(a) (b)

(a): 10 Hz (b): 60 Hz.

Gradient of pressures can be seen at the gas-water interfaces, stronger at 65 Hz than at 10 Hz. This Figure illustrates the mesoscopic less mechanism.

The effective shear modulus when the solid matrix is composed of two different materials.

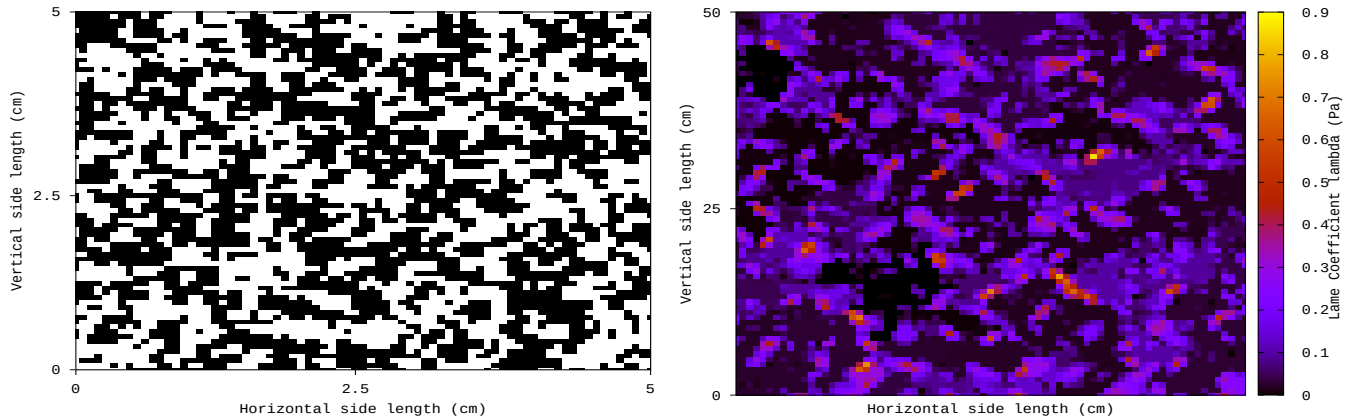

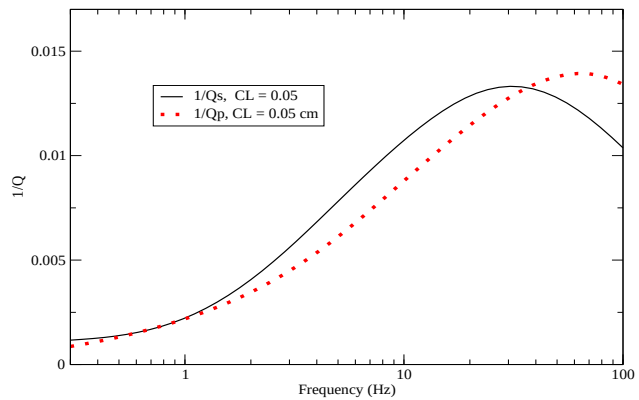

Top left: Fractal shale-sandstone 2 distribution. Black zones correspond to pure shale and white ones to pure sandstone 2. Shale percentage is 50 %. Top right: Absolute fluid pressure distribution (Pa) at 30 Hz. Bottom: Inverse quality factors Q_s and Q_p (the experiment is not included). Q_s of about 75 between 20 and 40 Hz, Q_p about 70 at 65 Hz. Conclusion: wave induced fluid flow is observed when shear and compressional waves propagate through Biot media with highly heterogeneous solid frames.

Fractured Biot media. I

- Fractures are common in the earth's crust due to different factors, for instance, tectonic stresses and natural or artificial hydraulic fracturing caused by a pressurized fluid.
- Seismic wave propagation through fractures and cracks is an important subject in exploration and production geophysics, earthquake seismology and mining.
- Fractures constitute the sources of earthquakes, and hydrocarbon and geothermal reservoirs are mainly composed of fractured rocks .

Fractured Biot media. II

- Modeling fractures requires a suitable interface model. Nakagawa and Schoenberg (JASA (2007)) presented a set of boundary conditions (B.C.) to represent fluid-solid interaction within a fracture and the effect of its permeability on seismic wave scattering.
- At a fracture, these B.C. impose: continuity of the total stress components, discontinuities of pressure (or pressures) -proportional to averaged fluid velocities across and discontinuities of displacements-proportional to stress components and averaged fluid pressures.
- They allow to represent wave-induced fluid flow (mesoscopic loss) by which the fast waves are converted to slow (diffusive) Biot waves when travelling across fractures.

Boundary conditions at a fracture inside a Biot medium. I

$\Omega = (0, L_1) \times (0, L_3)$ with boundary Γ in the (x_1, x_3)-plane, x_1, x_3: horizontal and vertical coordinates, respectively.

Ω contains a set of horizontal fractures $\Gamma^{(f,l)}, l = 1, \cdots, J^{(f)}$ each one of length L_1 and aperture $h^{(f)}$. This set of fractures divides Ω in a collection of non-overlapping rectangles $R^{(l)}, l = 1, \cdots, J^f + 1$.

Assume that the rectangles $R^{(l)}$ and $R^{(l+1)}$ have a fracture $\Gamma^{(f,l)}$ as a common side.

$[\mathbf{u}^s], [\mathbf{u}^f]$: jumps of the solid and fluid displacement vectors at $\Gamma^{(f,l)}$.

$\nu_{l,l+1}$ and $\chi_{l,l+1}$: the unit outer normal and a unit tangent (oriented counterclockwise) on $\Gamma^{(f,l)}$ from $R^{(l)}$ to $R^{(l+1)}$.

Boundary conditions at a fracture $\Gamma^{(f,l)}$ inside a Biot medium. II

$$[\mathbf{u}^s \cdot \nu_{l,l+1}] = \eta_N \left((1 - \alpha^{(f)} \widetilde{B}^{(f)} (1 - \Pi)) \tau(\mathbf{u}) \nu_{l,l+1} \cdot \nu_{l,l+1} - \alpha^{(f)} \frac{1}{2} \left((-p_f^{(l+1)}) + (-p_f^{(l)}) \right) \Pi \right),$$

$$[\mathbf{u}^s \cdot \chi_{l,l+1}] = \eta_T \, \tau(\mathbf{u}) \nu_{l,l+1} \cdot \chi_{l,l+1},$$

$$\left[\mathbf{u}^f \cdot \nu_{l,l+1} \right] = \alpha^{(f)} \eta_N \left(-\tau(\mathbf{u}) \nu_{l,l+1} \cdot \nu_{l,l+1} + \frac{1}{\widetilde{B}^{(f)}} \frac{1}{2} \left((-p_f^{(l+1)}) + (-p_f^{(l)}) \right) \right) \Pi,$$

$$(-p_f^{(l+1)}) - (-p_f^{(l)}) = \frac{\mathrm{i} \varnothing \mu^{(\mathrm{f})''}}{\widehat{\kappa}^{(f)}} \frac{1}{2} \left(\mathbf{u}_f^{(l+1)} + \mathbf{u}_f^{(l)} \right) \cdot \nu_{l,l+1},$$

$$\tau(\mathbf{u}) \nu_{l,l+1} \cdot \nu_{l,l+1} = \tau(\mathbf{u}) \nu_{l+1,l} \cdot \nu_{l+1,l},$$

$$\tau(\mathbf{u}) \nu_{l,l+1} \cdot \chi_{l,l+1} = \tau(\mathbf{u}) \nu_{l+1,l} \cdot \chi_{l+1,l},$$

η_N and η_T: normal and tangential fracture compliances.

Boundary conditions at a fracture $\Gamma^{(f,l)}$ inside a Biot medium. II

Fracture dry plane wave and shear modulus $H_m^{(f)} = K_m^{(f)} + \frac{4}{3}\mu^{(f)}$ and $\mu^{(f)}$ in terms of η_N, η_T:

$$\eta_N = \frac{h^{(f)}}{H_m^{(f)}}, \qquad \eta_T = \frac{h^{(f)}}{\mu^{(f)}}.$$

$$\alpha^{(f)} = 1 - \frac{K_m^{(f)}}{K_s^{(f)}}, \qquad \widehat{\kappa}^{(f)} = \frac{\kappa^{(f)}}{h^{(f)}},$$

$$\epsilon = \frac{(1+\mathrm{i})}{2}\left(\frac{\varnothing\,\eta^{(f)}\,\alpha^{(f)}\,\eta_N}{2\,\widetilde{B}^{(f)}\,\widehat{\kappa}^{(f)}}\right)^{1/2}, \quad \Pi(\epsilon) = \frac{\tanh\epsilon}{\epsilon},$$

$$\widetilde{B}^{(f)} = \frac{\alpha^{(f)} M^{(f)}}{H_u^{(f)}}, \quad H_u^{(f)} = K_u^{(f)} + \frac{4}{3}\mu^{(f)}.$$

A TIV medium equivalent to a Biot's medium with aligned fractures. I

- A Biot medium with a dense set of horizontal fractures behaves as a Transversely Isotropic and Viscoelastic (TIV) medium when the average fracture distance is much smaller than the predominant wavelength of the travelling waves.
- This leads to frequency and angular variations of velocity and attenuation of seismic waves.
- The time-harmonic experiments described before are generalized and applied to determine the TIV medium long-wave equivalent to a densely fractured Biot medium.

A TIV medium equivalent to a Biot's medium with aligned fractures. II

$\widetilde{\sigma}_{ij}(\widetilde{\vec{u}}^s)$, $e_{ij}(\widetilde{\vec{u}}^s)$: stress and strain tensor components of the equivalent TIV medium

$\widetilde{\vec{u}}^s$: solid displacement vector at the macro-scale.

The TIV stress-strain relations:

$$\begin{aligned}
\widetilde{\sigma}_{11}(\widetilde{\vec{u}}^s) &= p_{11}\ e_{11}(\widetilde{\vec{u}}^s) + p_{12}\ e_{22}(\widetilde{\vec{u}}^s) + p_{13}\ e_{33}(\widetilde{\vec{u}}^s),\\
\widetilde{\sigma}_{22}(\widetilde{\vec{u}}^s) &= p_{12}\ e_{11}(\widetilde{\vec{u}}^s) + p_{11}\ e_{22}(\widetilde{\vec{u}}^s) + p_{13}\ e_{33}(\widetilde{\vec{u}}^s),\\
\widetilde{\sigma}_{33}(\widetilde{\vec{u}}^s) &= p_{13}\ e_{11}(\widetilde{\vec{u}}^s) + p_{13}\ e_{22}(\widetilde{\vec{u}}^s) + p_{33}\ e_{33}(\widetilde{\vec{u}}^s),\\
\widetilde{\sigma}_{23}(\widetilde{\vec{u}}^s) &= 2\ p_{55}\ e_{23}(\widetilde{\vec{u}}^s),\\
\widetilde{\sigma}_{13}(\widetilde{\vec{u}}^s) &= 2\ p_{55}\ e_{13}(\widetilde{\vec{u}}^s),\\
\widetilde{\sigma}_{12}(\widetilde{\vec{u}}^s) &= 2\ p_{66}\ e_{12}(\widetilde{\vec{u}}^s).
\end{aligned}$$

$$p_{22} = p_{11}, \quad p_{23} = p_{13}, \quad p_{55} = p_{44}, p_{12} = p_{11} - 2p_{66}.$$

A TIV medium equivalent to a Biot's medium with aligned fractures. III

- In the context of Numerical Rock Physics the complex stiffness coefficients p_{IJ} are determined using five time-harmonic experiments, each one associated with a BVP.
- The BVP's consist on compressibility and shear tests on a sample of Biot material with a dense set of fractures modeled using B. C..
- The BVP's are formulated in the space-frequency domain and solved using th FEM.
- This approach offers an alternative to laboratory measurements. It is essentially free from experimental errors and can easily be run using alternative models of the materials being analized.

The Experiments to Deterime the Five p_{IJ} TIV Stiffness

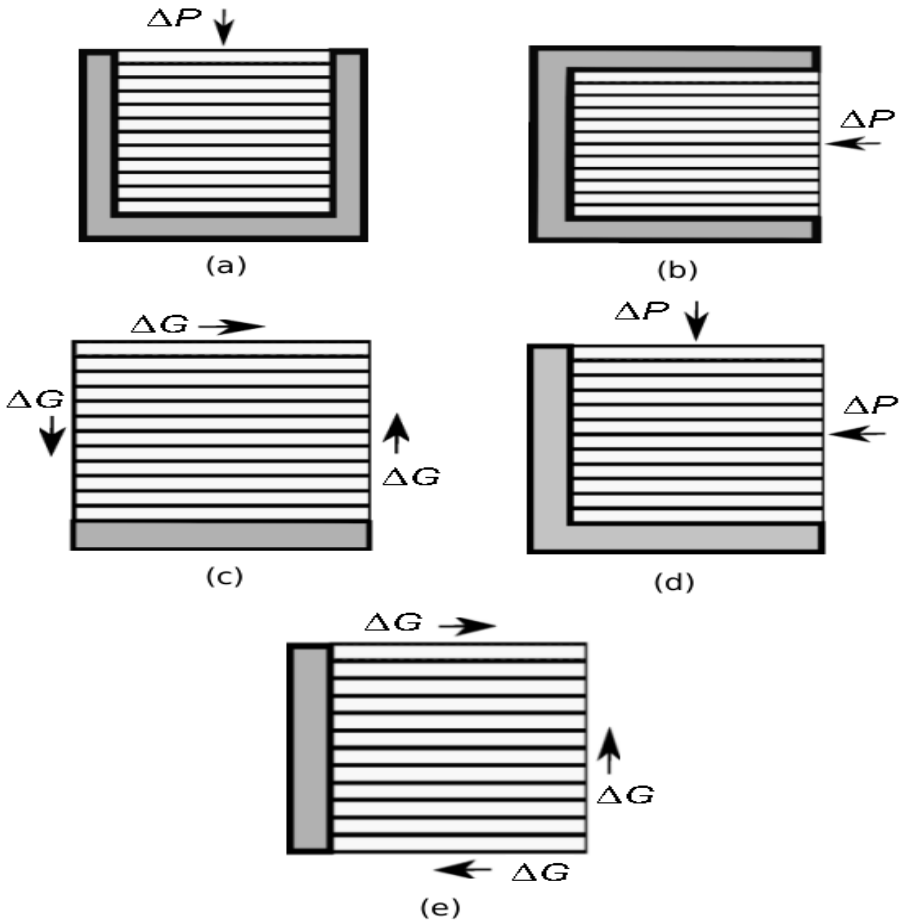

(I) : Figures (a) and (b) show how to determine p_{33} and p_{11}, (c) determines p_{55}, (e) determines p_{66} and (d) determines p_{13}.

Numerical Experiments. I

The procedure to determine the complex stiffnesses $p_{IJ(\omega)}$ at the macro-scale was validated by comparison with the analytical solution given by Krzikalla and Müller (GPY, 2011).

Next were applied to patchy brine-gas saturation, a case for which no analytical solutions are avalaible.

Instead of the stiffnesses $p_{IJ(\omega)}$ the Figures display the the corresponding energy velocities and dissipation coefficients.

In all the experiments we used square samples of side length 2 m, with 9 fractures at equal distance of 20 cm and fracture aperture 1 mm.

The numerical samples were discretized with a 100×100 uniform mesh.

Material Properties of background and fractures.

Table: Material properties of background and fractures

Background	Solid grains bulk modulus, K_s	36. GPa
	solid grains density, ρ_s	2700 kg/m^3
	Dry bulk modulus K_m	9 GPa
	shear modulus G	7 GPa
	Porosity ϕ	0.15
	permeability κ	0.1 Darcy
Fractures	Solid grains bulk modulus, K_s	36. GPa
	solid grains density, ρ_s	2700 kg/m^3
	Dry bulk modulus K_m	0.0055 GPa
	shear modulus G	0.0033 GPa
	Porosity ϕ	0.5
	permeability κ	10 Darcy

The properties of the saturant fluids, brine and gas, are the same than in the previous example for patchy saturation.

qP and qSV energy velocity at 30 Hz for full brine, full gas, 10% and 50% patchy gas-brine saturation.

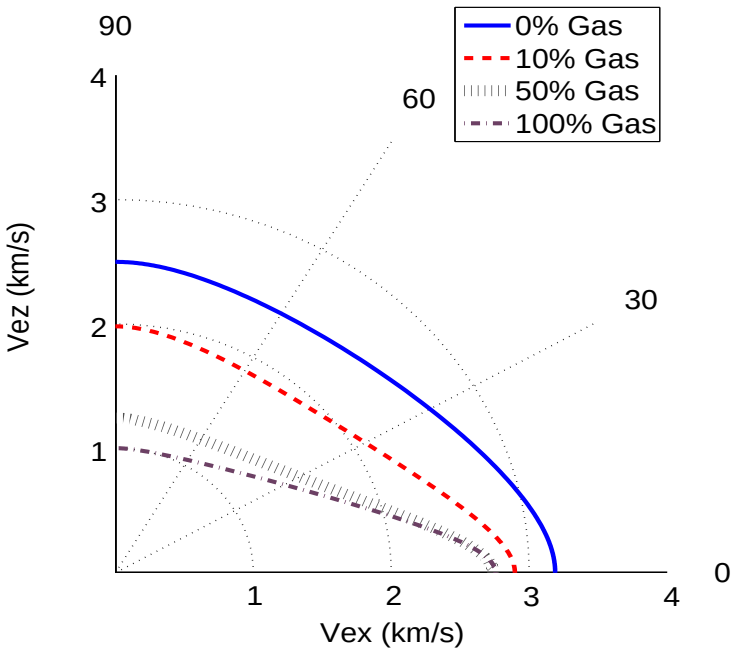

(a)

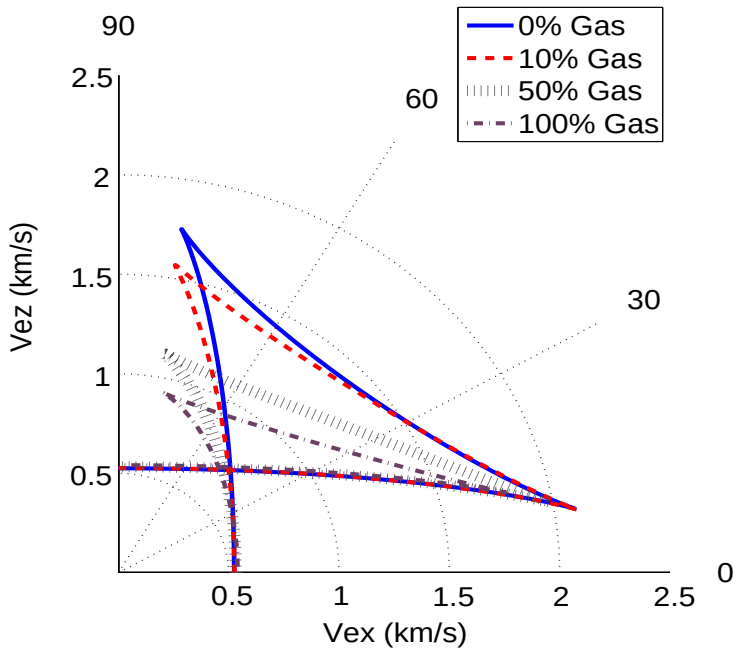

(b)

(a) : qP energy velocity (b) : qSV energy velocity. qP and qSV velocity decreases as gas saturation increases. qSV velocity exhibits the typical cuspidal triangles.

qP and qSV dissipation factors at 30 Hz for full brine, full gas, 10% and 50% patchy gas-brine saturation.

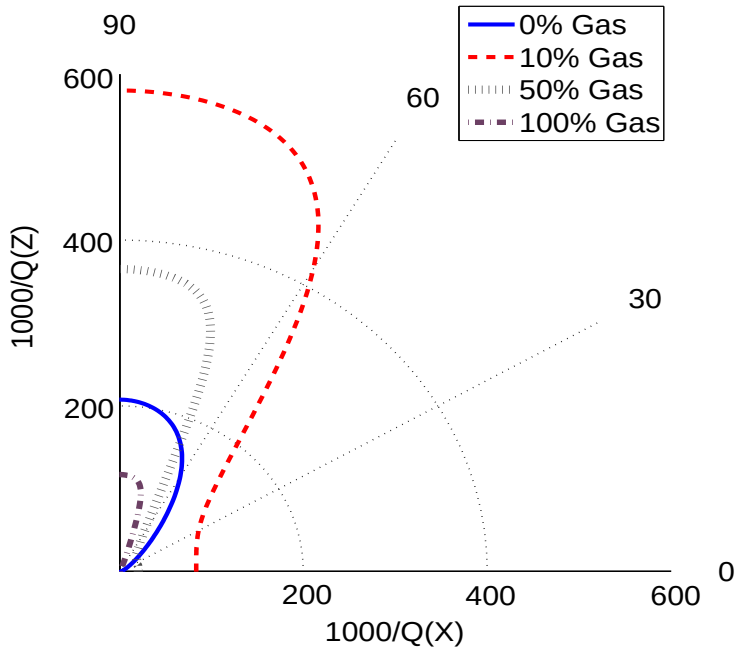

(a)

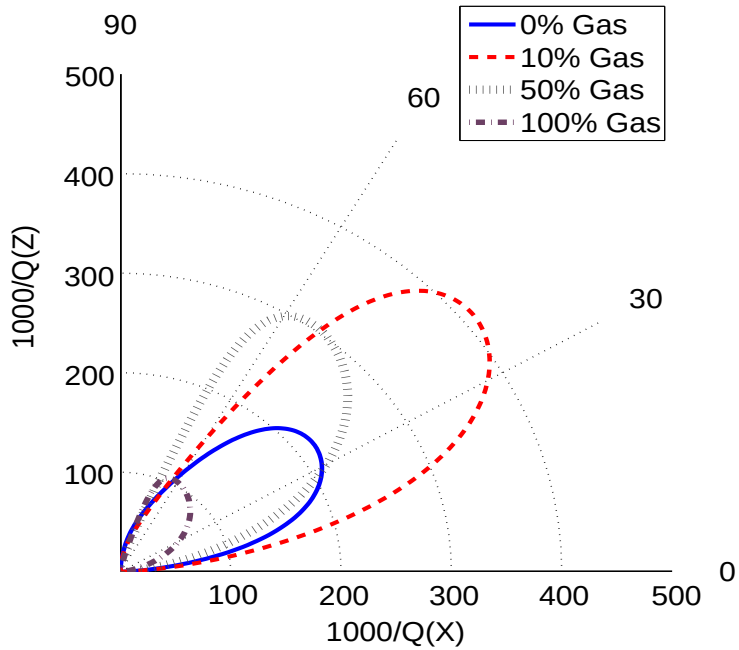

(b)

(a) : $\frac{1000}{qP}$ (b) : $\frac{1000}{qSV}$.

qP anisotropy is enhanced by patchy saturation, is highest at 10 % gas saturation and with maximums for waves arriving normally to the fracture layering. qSV waves show maximum attenuation at 10 % gas saturation, with different anisotropic behaviour depending on gas saturation.

SH energy velocity at 30 Hz for full brine saturation. The SH polarization is normal to the plane (x_1, x_3) that is the plane of the figure

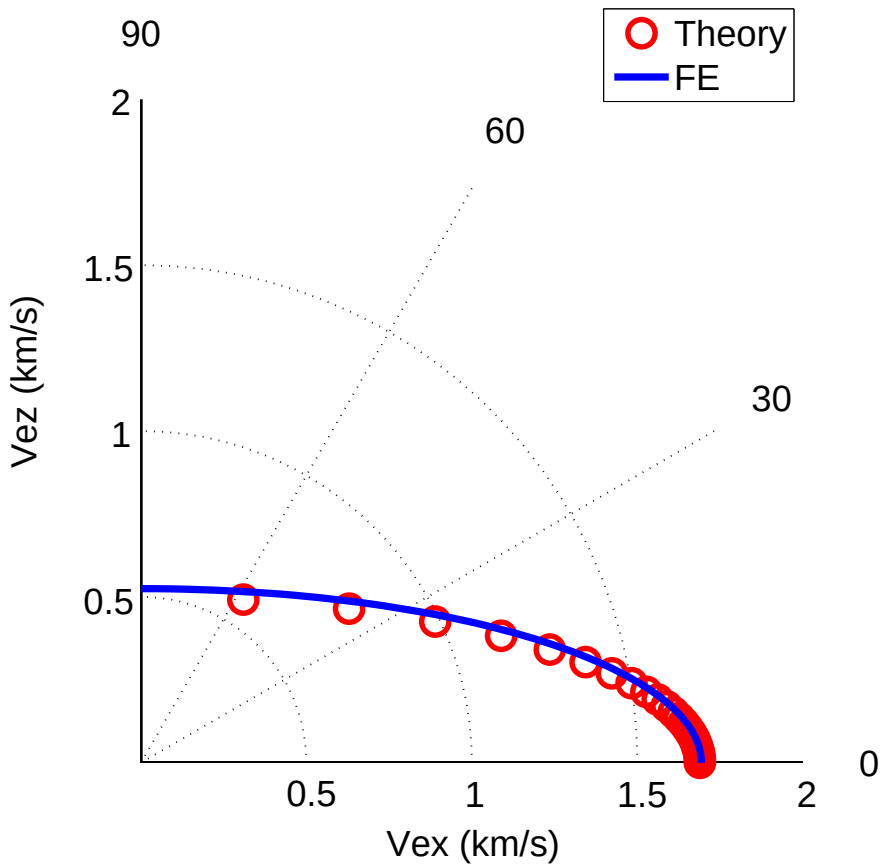

SH waves show velocity anisotropy and they are lossless

Fluid pressure for normal compression to the fracture plane at 30 Hz and 10 % patchy gas saturation.

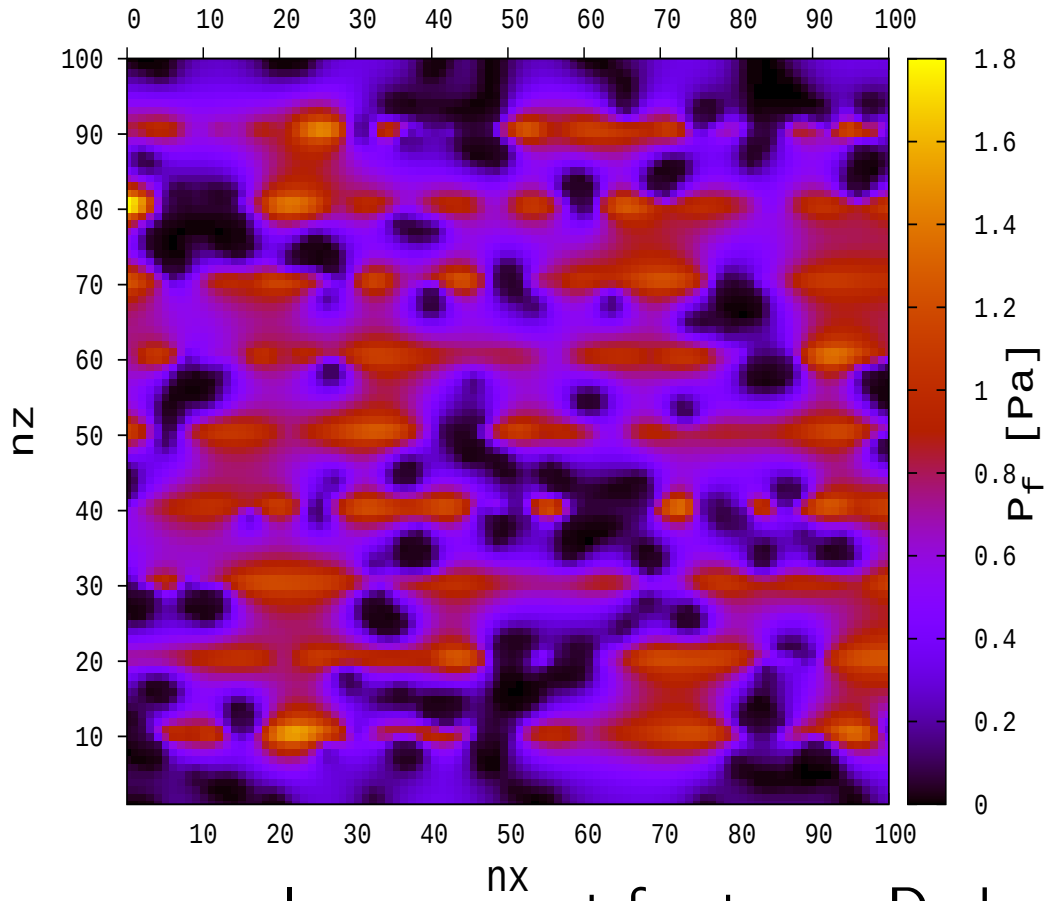

Higher pressure values occur at fractures. Darker regions identify gas patches. High pressure gradients at boundaries of fractures and patches show the mesoscopic loss effect.

The macro-scale. Seismic monitoring of CO_2 sequestration. I

- Capture and storage of carbon dioxide in deep saline aquifers and aging oil reservoirs is a valid alternative approach for reducing the amount of greenhouse gases in the atmosphere
- We model CO_2 injection in the Utsira formation at the Sleipner gas field in the North Sea.
- Within the formation, there are several mudstone layers acting as barriers to the vertical flow of CO_2. Injection started in 1996 at a rate of about one million tonnes per year.
- A petrophysical model of the Utsira formation is built based on fractal porosity and clay content, taking into account the variation of properties with pore pressure and saturation.

The macro-scale. Seismic monitoring of CO_2 sequestration. II

- We describe a methodology to model the CO_2 flow and monitor the storage combining numerical simulations of CO_2-brine flow and seismic wave propagation.
- Flow of brine and CO_2 is modeled with the Black-Oil formulation for two-phase flow in porous media.
- A space-frequency domain wave propagation simulator is used to monitor the injection. A Zener model is used to determine the P and S waves moduli in the brine saturated zones.
- In zones where CO_2 is present, patchy CO2-brine distribution is assumed and the time-harmonic compressibility tests are used to model P-wave velocity and attenuation. The S modulus is determined using a mechanism related to the P-modulus.

A petrophysical model for the Utsira formation. I

The pressure dependence of properties is based on the following relationship between porosity and pore pressure $p(t) = S_b p_b(t) + S_g p_g(t)$:

$$\frac{(1-\phi_c)}{K_s}(p(t) - p_H) = \phi_0 - \phi(t) + \phi_c \ln \frac{\phi(t)}{\phi_0}$$

S_b, S_g: brine and CO_2 saturations, ϕ_c: a critical porosity $\phi_0 = \phi_0(x, z)$: initial porosity at hydrostatic pore pressure p_H, assumed to have a fractal spatial distribution around the average porosity $\langle \phi_0 \rangle$, obtained from the neutron log. K_s: bulk modulus of the solid grains, computed as the arithmetic average of the Hashin Shtrikman upper and lower bounds of quartz (bulk modulus of 40 GPa) and clay (bulk modulus of 15 GPa).

A petrophysical model for the Utsira formation. II

Relationship among horizontal permeability (κ_{x_1}), porosity and clay content (C):

$$\frac{1}{\kappa_{x_1}(t)} = \frac{45(1-\phi(t))^2}{\phi(t)^3}\left(\frac{(1-C)^2}{R_q^2} + \frac{C^2}{R_c^2}\right),$$

R_q, R_c: average radii of the sand and clay grains, respectively. Assumed relation between the horizontal and vertical permeabilities $\kappa_{x_1}, \kappa_{x_3}$:

$$\frac{\kappa_{x_1}(t)}{\kappa_{x_3}(t)} = \frac{1-(1-0.3a)\sin(\pi S_b)}{a(1-0.5\sin(\pi S_b))},$$

a: permeability-anisotropy parameter (a= 0.1 here)).
The bulk and shear moduli of the dry matrix, K_m, μ_m are computed using the Krief model:

$$K_m(t) = K_s(1-\phi(t))^{A/(1-\phi(t))},$$
$$\mu_m(t) = \mu_s(1-\phi(t))^{A/(1-\phi(t))}$$

A petrophysical model for the Utsira formation. III

Using the moduli K_s, μ_s, K_m, μ_m,porosity ϕ and permeabilities κ_x, κ_z, the fluids bulk moduli and viscosities and the CO_2 saturation map we determine the complex and frequency dependent P-wave and S moduli at each computational cell using the harmonic experiments.
The flow simulator model uses the following relative permeabilities and capillary pressure functions:

$$K_{rg}(S_g) = K^*_{rg}\left(\frac{S_g - S_{gc}}{1 - S_{gc} - S_{bc}}\right)^{n_g}$$

$$K_{rb}(S_g) = K^*_{rb}\left(\frac{1 - S_g - S_{bc}}{1 - S_{gc} - S_{bc}}\right)^{n_b},$$

$$P_{ca}(S_g) = P^*_{ca}\left(\frac{S_g - S_{gc}}{1 - S_{gc} - S_{bc}}\right)^{n_c}.$$

S_{gc} and S_{bc}: saturations at which the CO_2 and brine phases become mobile.

Modeling CO_2 injection. I

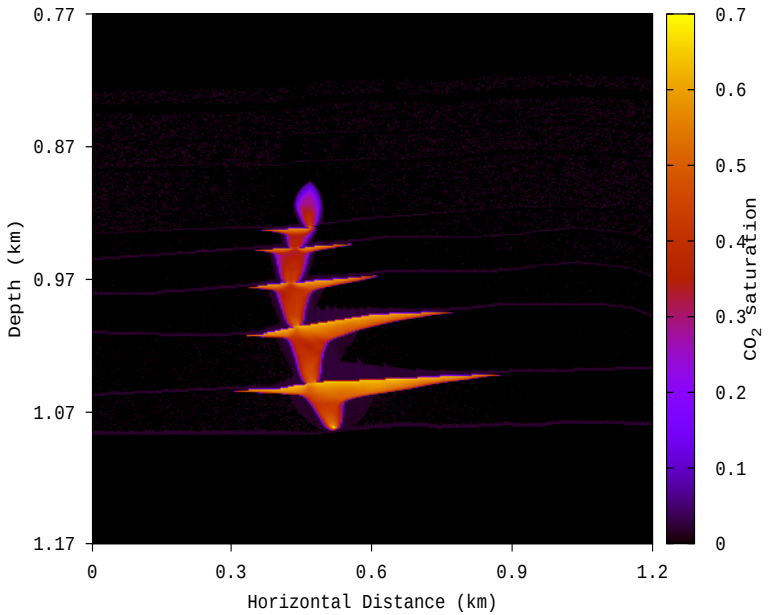

(a) CO_2 saturation after 1 year of injection

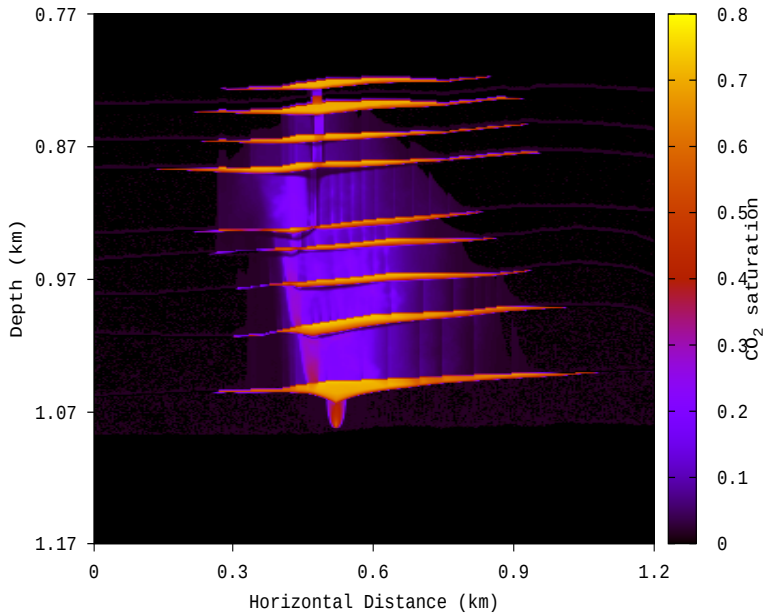

(b) CO_2 saturation after 3 years of injection

CO_2 is seen to move upwards and accumulate below the mudstone layers.

Modeling CO_2 injection. II

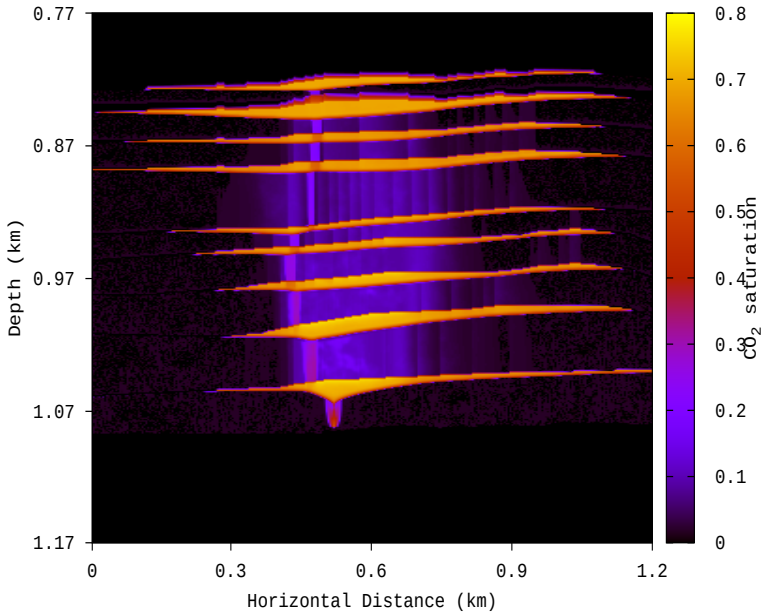

(a) CO_2 saturation after 7 years of injection

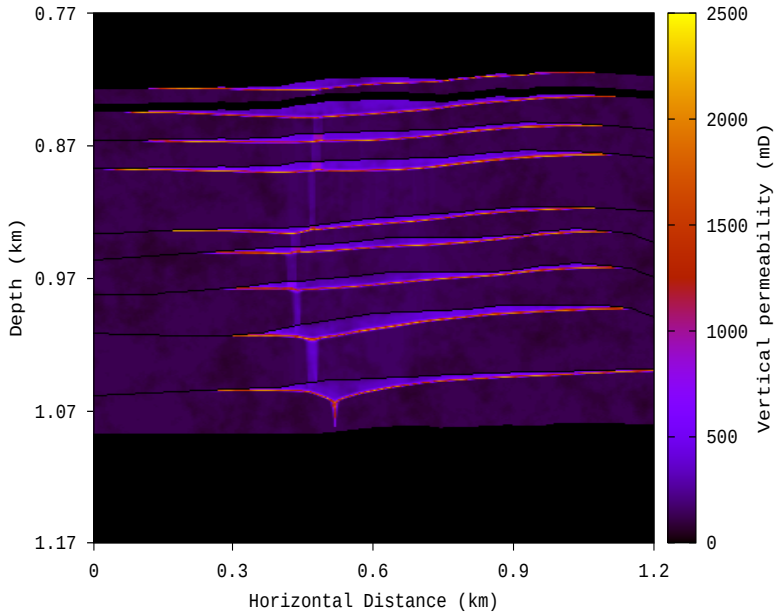

(b) Vertical permeability distribution after seven ye

In Figure a) CO_2 continues to move upwards and accumulate below the mudstone layers. Figure b) shows the updated saturation dependent vertical permeability.

Time-lapse seismics applied to monitor CO_2 sequestration. I

- We use 2-D slices of CO_2 saturation and fluid pressure maps obtained from the flow simulator to construct a 2-D model of the Utsira formation. The mesh is 600 cells in the x_1-direction and 200 cells in the x_3-direction.
- The seismic source is a spatially localized plane wave of main frequency 60 Hz located at $z = 772$ m. A line of receivers is located at the same depth to record the Fourier transforms of the vertical displacements.
- The plane-wave simulation (a flat line of point sources at each grid point at the surface) is a good approximation to the stack.

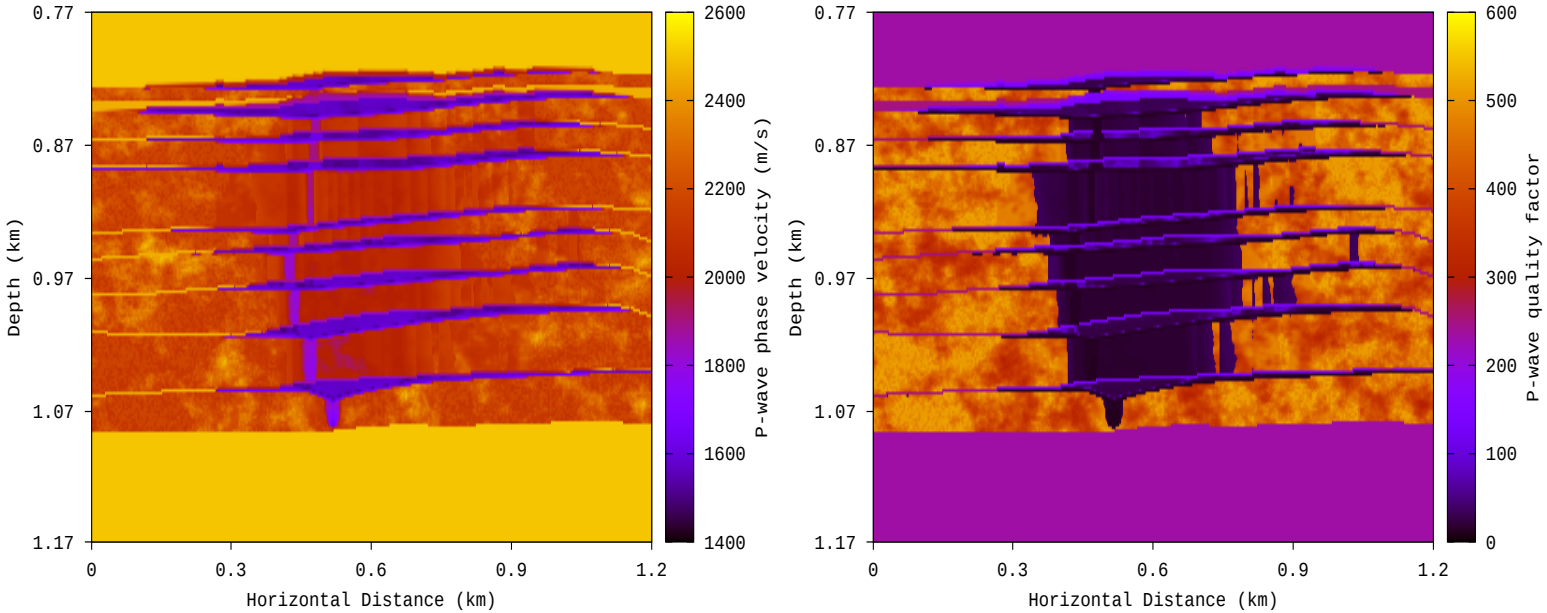

(a) v_p map at 50 Hz after 7 years of CO_2 injection (b) Q_P map at 50 Hz after 7 years of CO_2 injection

This Figures show how the injected CO_2 change P-wave velocities and quality factors v_p and Q_p; both decrease in the CO_2-saturated zones. A lower value of Q_p indicates a higher attenuation.

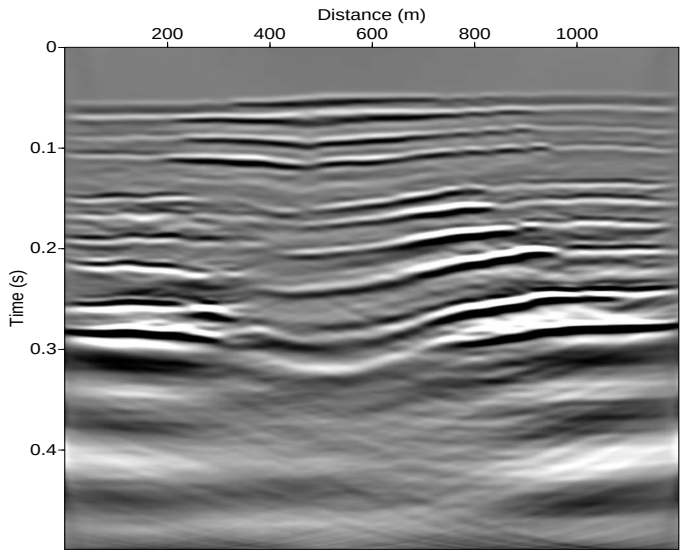

(a) Seismogram after 3 years of CO_2 injection.

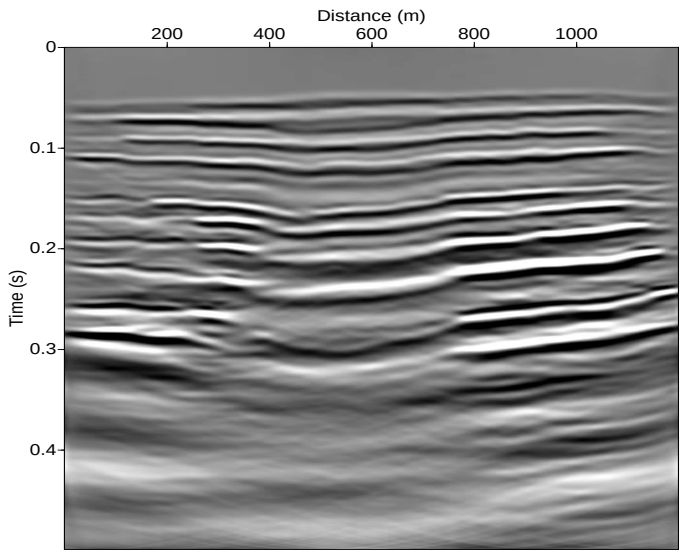

(b) Seismogram after 7 years of CO_2 injection.

Figures a) and b) show how CO_2 modes upwards and accumulates below the mudstone layers. the pushdown effect is clearly observed

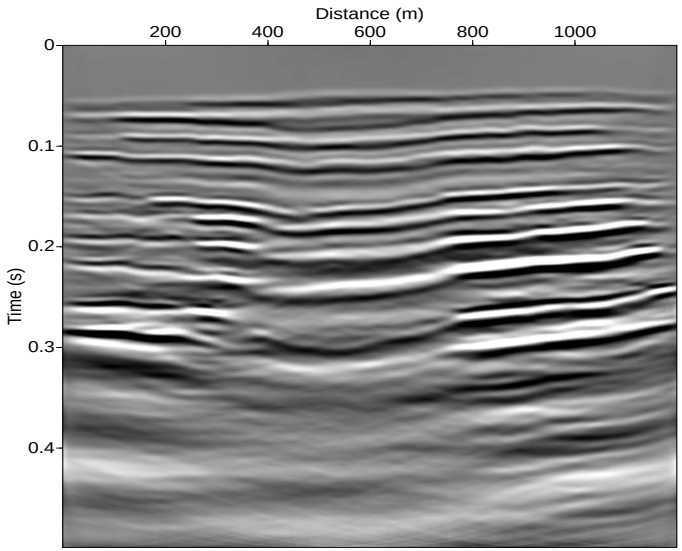

(a) Seismogram after 3 years of CO_2 injection.

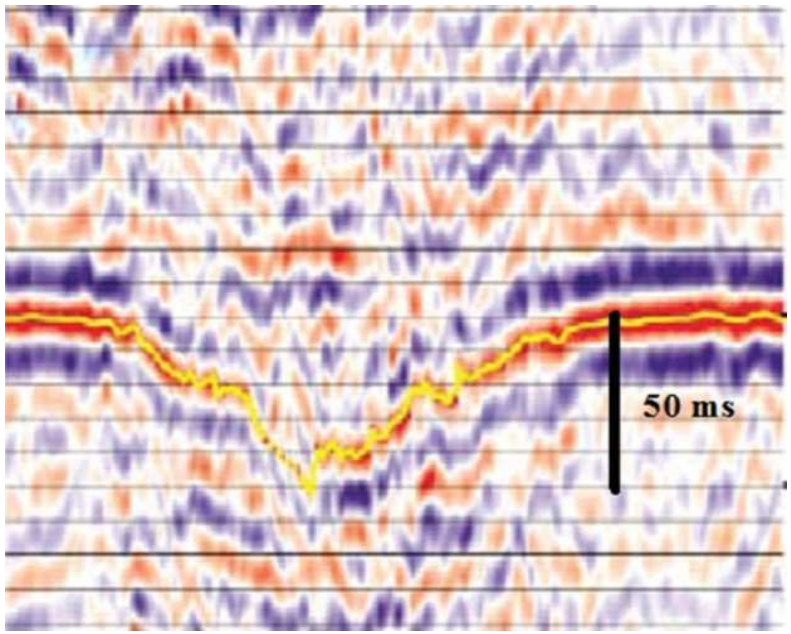

(b) Seismogram after 7 years of CO_2 injection.

Figures a) and b) show the delay in the arrival times of the reflections, the pushdown effect and the strong attenuation in the chimney region observed in real seismograms. The delay has been properly matched in the simulations.

3D VTI wave fronts. Full brine saturation in background and fractures. The source is compressional and located at the center of the domain.

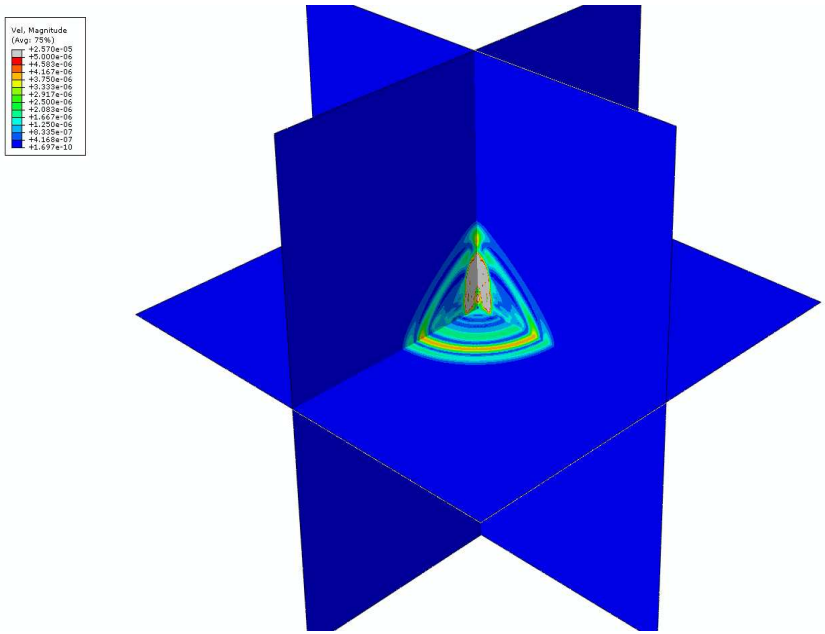

Figure 48 (a) 100 ms

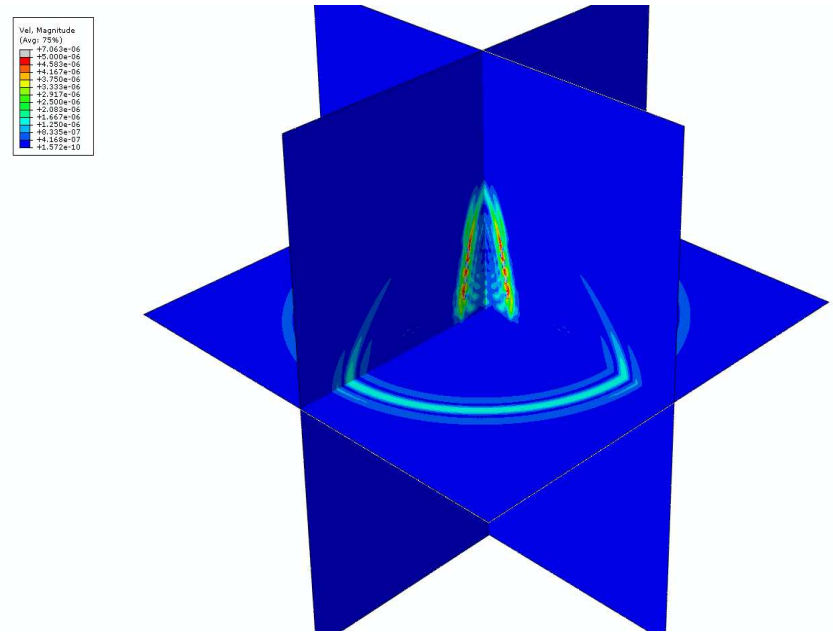

Figure 48 (b) 200 ms

qP and qSV waves propagate in the (x, z) and (y, z) anisotropic planes, which are normal to the fracture layering plane (x, y) (OK)

The qP wavefronts are the faster and are highly attenuated as indicated in the curves in Figures 33 (a) and 34 (a). (OK)

qSV wavefronts move much faster in the direction z normal to the fracture layering, as shown in Figure 33 (b). (FALSO)

Attenuation of qSV waves is low in the directions parallel (x) and normal (z) to the fracture layering, as seen in Figure 34 (b), so qSV wavefronts are clearly seen in these snapshots.

A P-wavefront is propagating in the isotropic (x, y)-plane.(OK)

2D VTI wave fronts in the (x, z)-plane. Full brine saturation in background and fractures. The source is compressional and located at the center of the domain

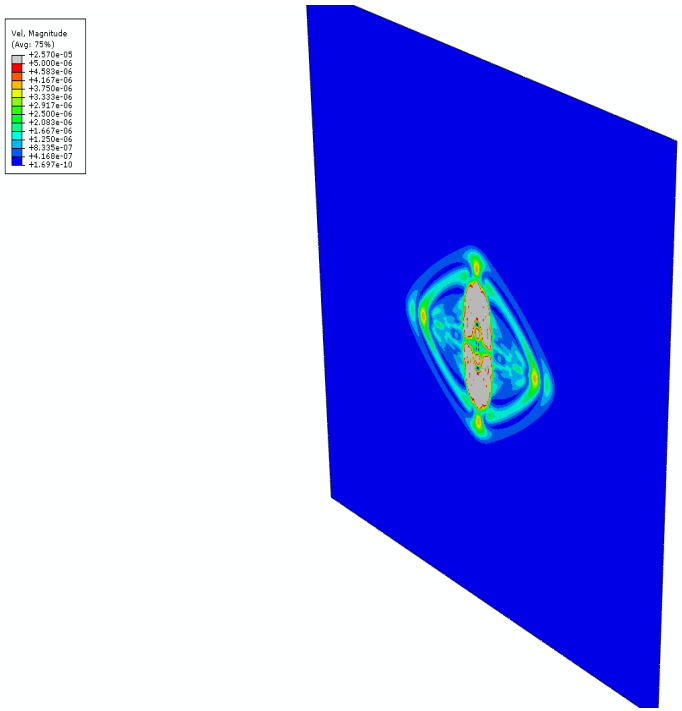

Figure 49 (a) 100 ms

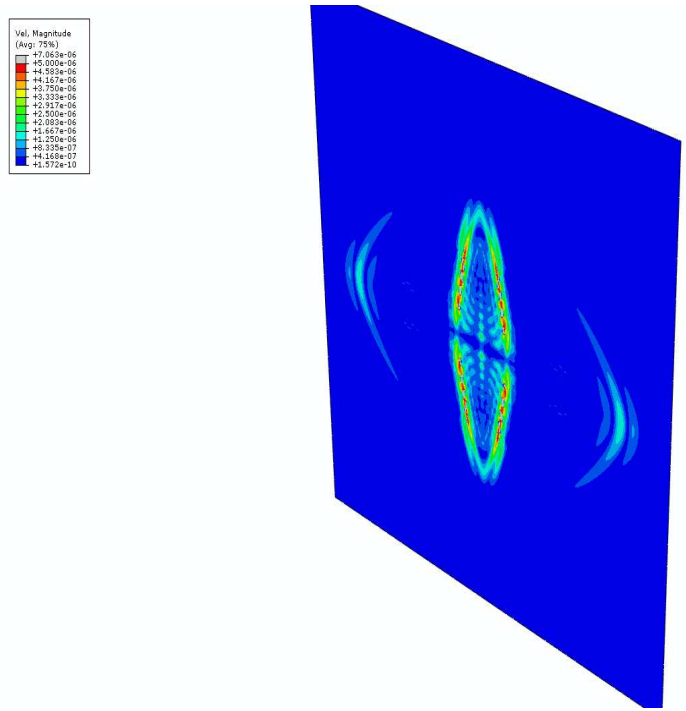

Figure 49 (b) 200 ms

qP and qSV wave fronts are seen to propagate in the (x, z) anisotropic plane, which is normal to the fracture layering plane x, y)

The qP wavefronts are the faster and are highly attenuated as indicated in the curves in Figures 33 (a) and 34 (a). qSV wavefronts move much faster in the direction z normal to the fracture layering, as shown in Figure 33 (b). Attenuation of qSV waves is low in the directions parallel (x) and normal (z) to the fracture layering, as seen in Figure 34 (b), so qSV wavefronts are clearly seen in these snapshots.

2D VTI wave fronts in the isotropic (x, y)-plane. Full brine saturation in background and fractures. The source is compressional and located at the center of the domain

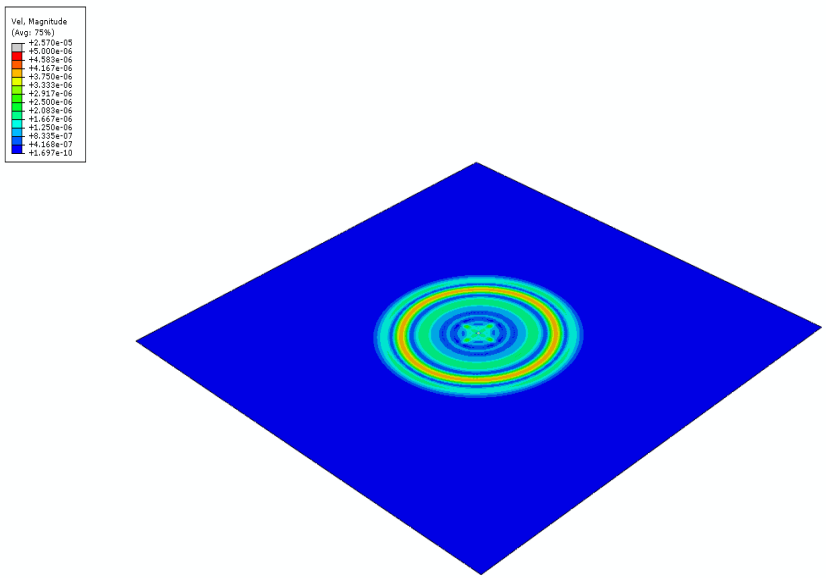

Figure 50 (a) 100 ms

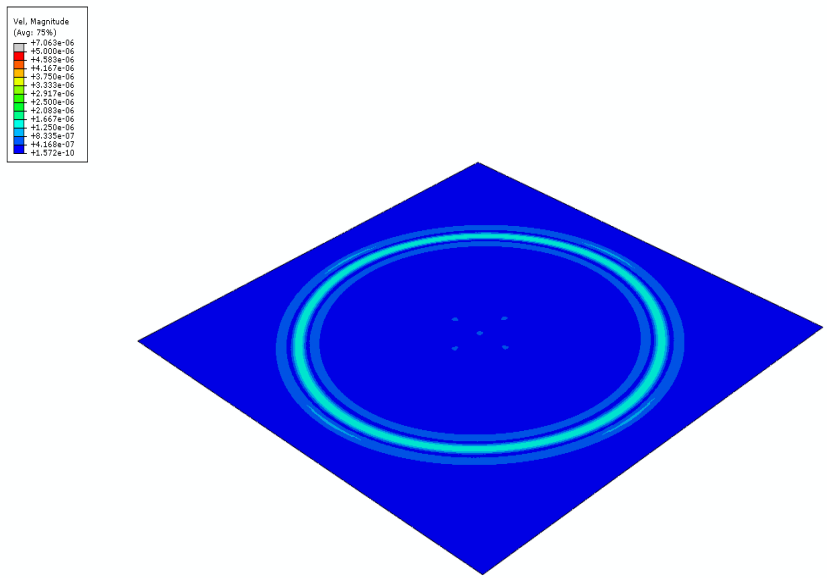

Figure 50 (b) 200 ms

An isotropic P-wavefront is seen traveling in the x, y) plane.

Snapshots of x-component of VTI displacements in (x, z)-plane. Full brine saturation.

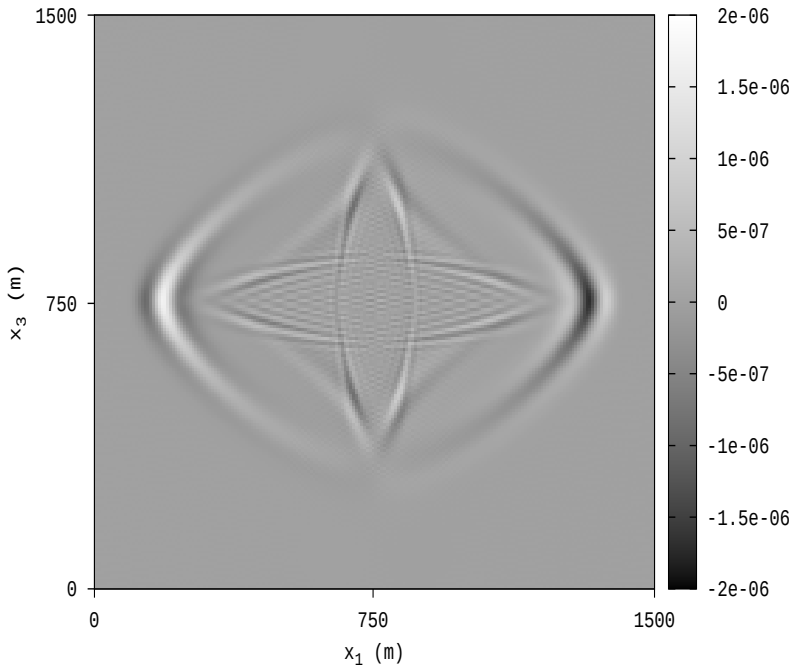

(a)

Figure 51 (a) : 200 ms

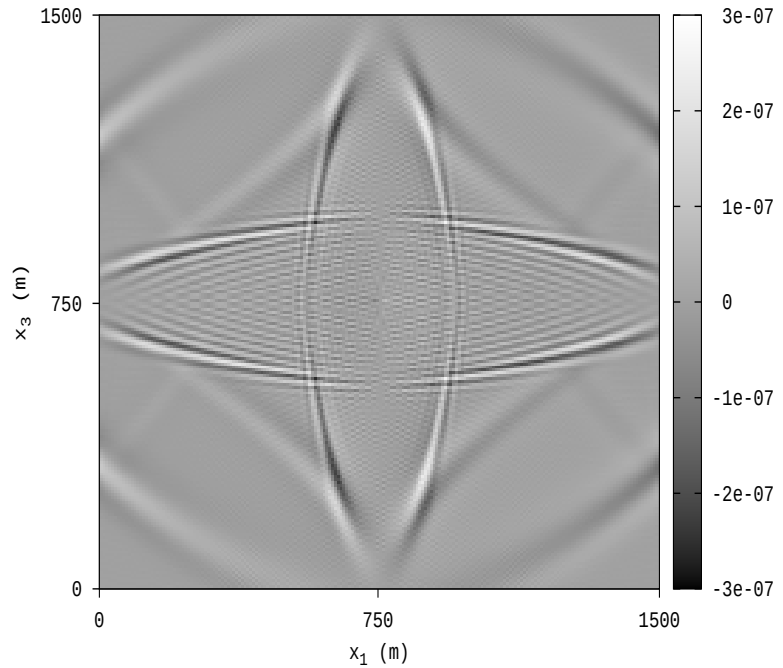

(b)

Figure 51 b) 300 ms

The faster wave front correspond to the qP wave, that moves faster in the horizontal than in the vertical direction, in accordance with the velocity graphs in Figure 33 a). The qSV wave shows vertical and horizontal wavefronts as well as the typical cusps (energy triplication) in the triangular wavefronts at 45 degrees, as indicated in Figure 33 b).

At 300 ms the qP wavefront in Figure 51 b) is already leaving the computational domain, while the qSV wavefronts are arriving to the artifical boundaries. Note that the absorbing boundary conditions for TIV media are working quite well, no spurious reflections from the artificial boundaries are observed. .

Snapshots of x-component of VTI displacements at 200 ms in (x, z)-plane. Full brine versus 10% patchy gas-brine saturation

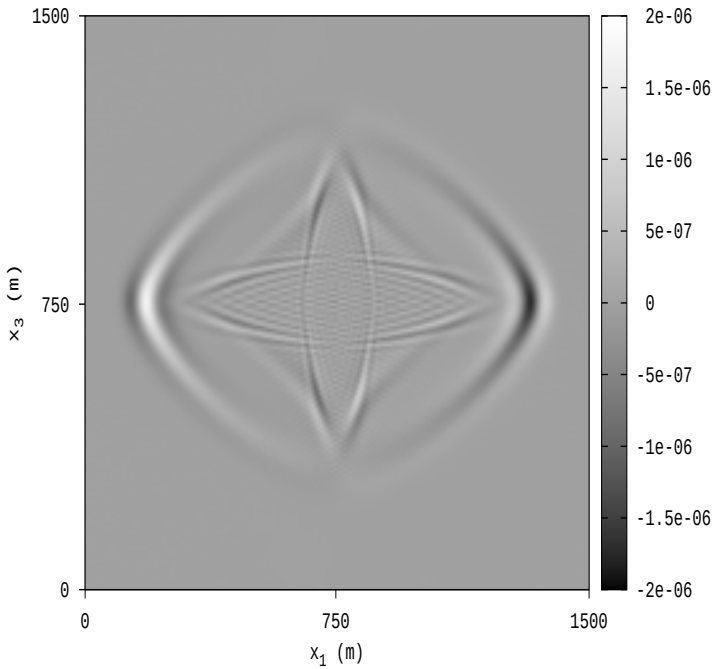

Figure 52 (a)

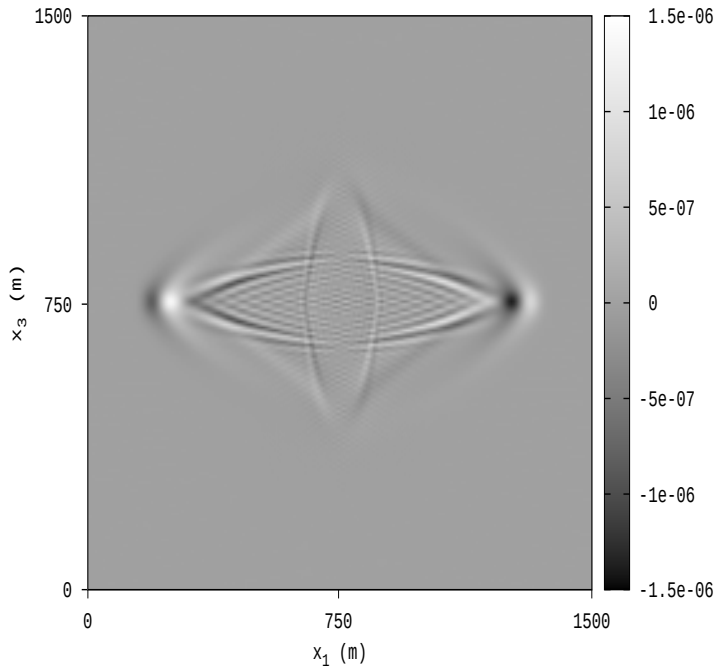

Figure 52 (b)

Figure 52 (a) : Brine saturation in background and fractures, Figure 52 (b) : Patchy gas-brine saturation in background and fractures with 10% overall gas saturation
The fast wave front in Figure 52 a) corresponds to the qP wave, that it is not seen in 52 b) because of the high attenuation of this wave in direction normal to the fracture layering (see Figure 34 a). qSV wavefronts in Figure 52 b) move slowly and more attenuated than in Figure 52 a), in accordance with the velocity and attenuation graphs in Figures 33 b) and 34 b)

Snapshots of x-component of VTI displacements at 300 ms in (x, z)-plane. Full brine versus 10% patchy gas-brine saturation.

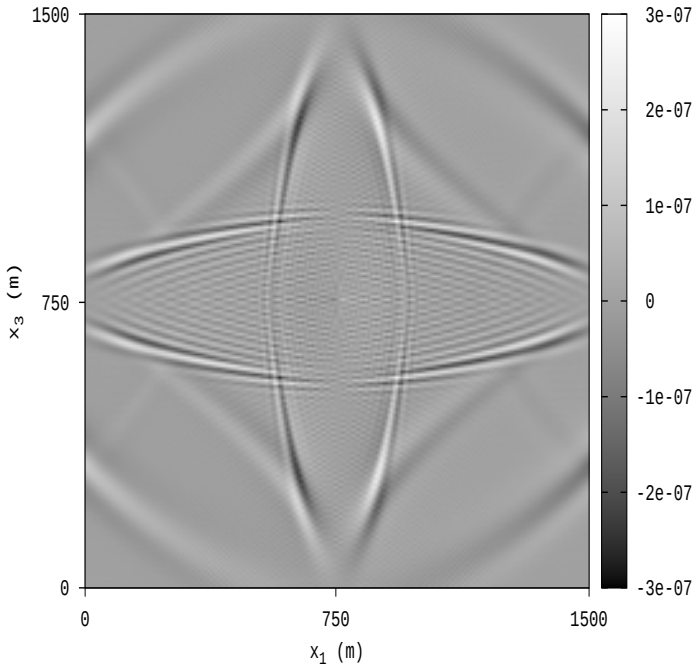

Figure 53 (a)

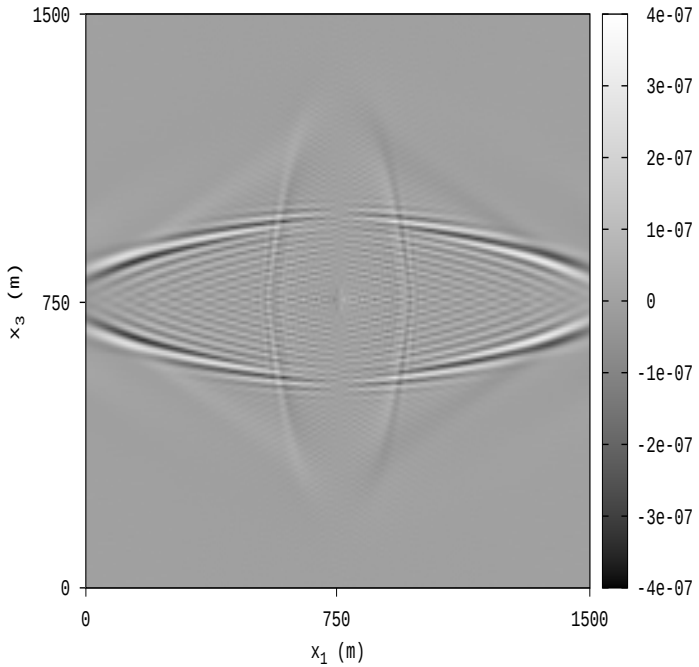

Figure 53 (b)

Figure 53 (a) : Brine saturation, Figure 53 (b) : Patchy gas-brine saturation in background and fractures, gas saturation is 10%.

The fast wave front in Figure 52 a) corresponds to the qP wave, that it is not seen in 52 b) because of the high attenuation of this wave in direction normal to the fracture layering (see Figure 34 a). qSV wavefronts in Figure 52 b) still show the triplication cusps and move slowly and more attenuated than in Figure 52 a), according with the graphs in Figures 33 b) and 34 b).

Snapshots of x-component of VTI displacements at 200 ms in (x, z)-plane. Full brine versus 50% patchy gas-brine saturation.

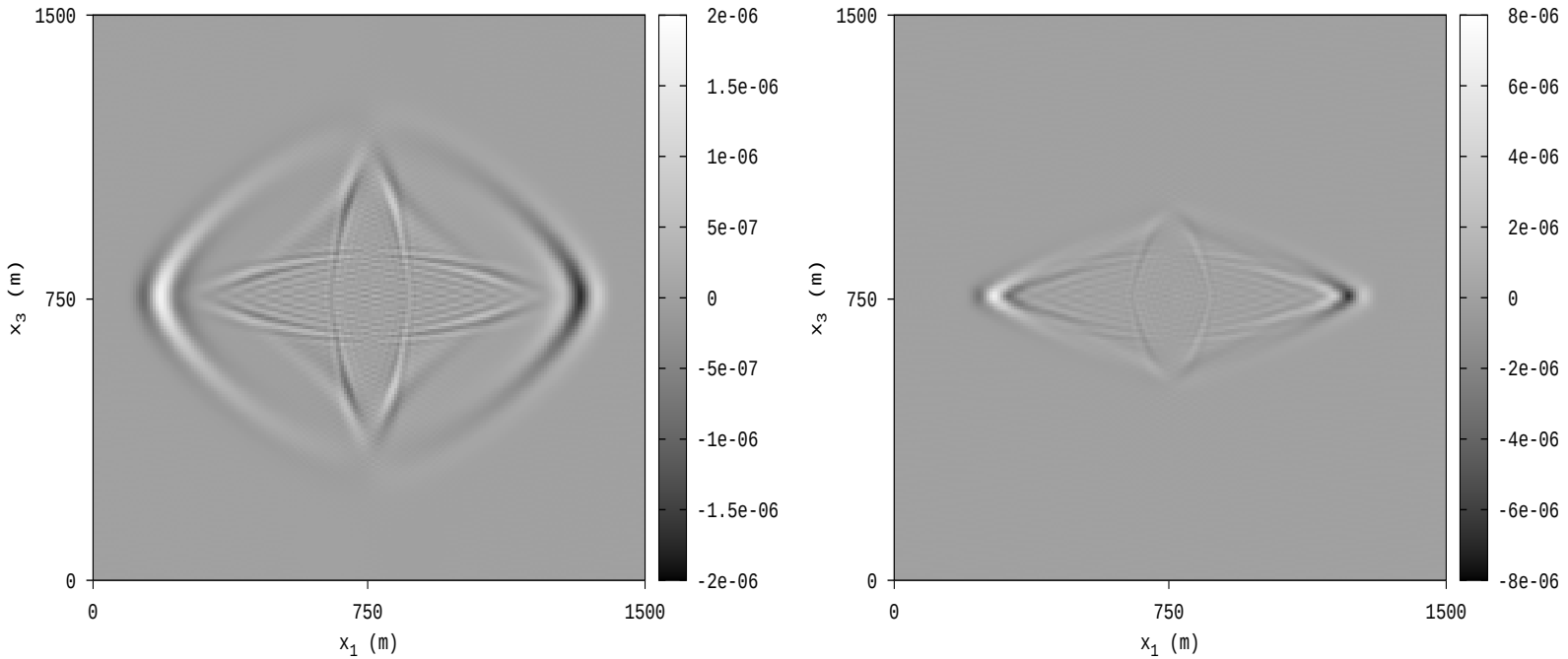

(a) (b)

Figure 54 (a) : Full brine saturation, Figure 54 (b) : Patchy gas-brine saturation in background and fractures with 50% overall gas saturation.

qSV wavefronts in Figure 54 b) are not as well defined as in the case of 10% patchy gas-brine saturation in 52 b). The triangular cusps are still present close to the vertical direction but not as well defined as in Figure 54 a).

Snapshots of x-component of VTI displacements at 300 ms in (x, z)-plane. Full brine versus 50% patchy gas-brine saturation.

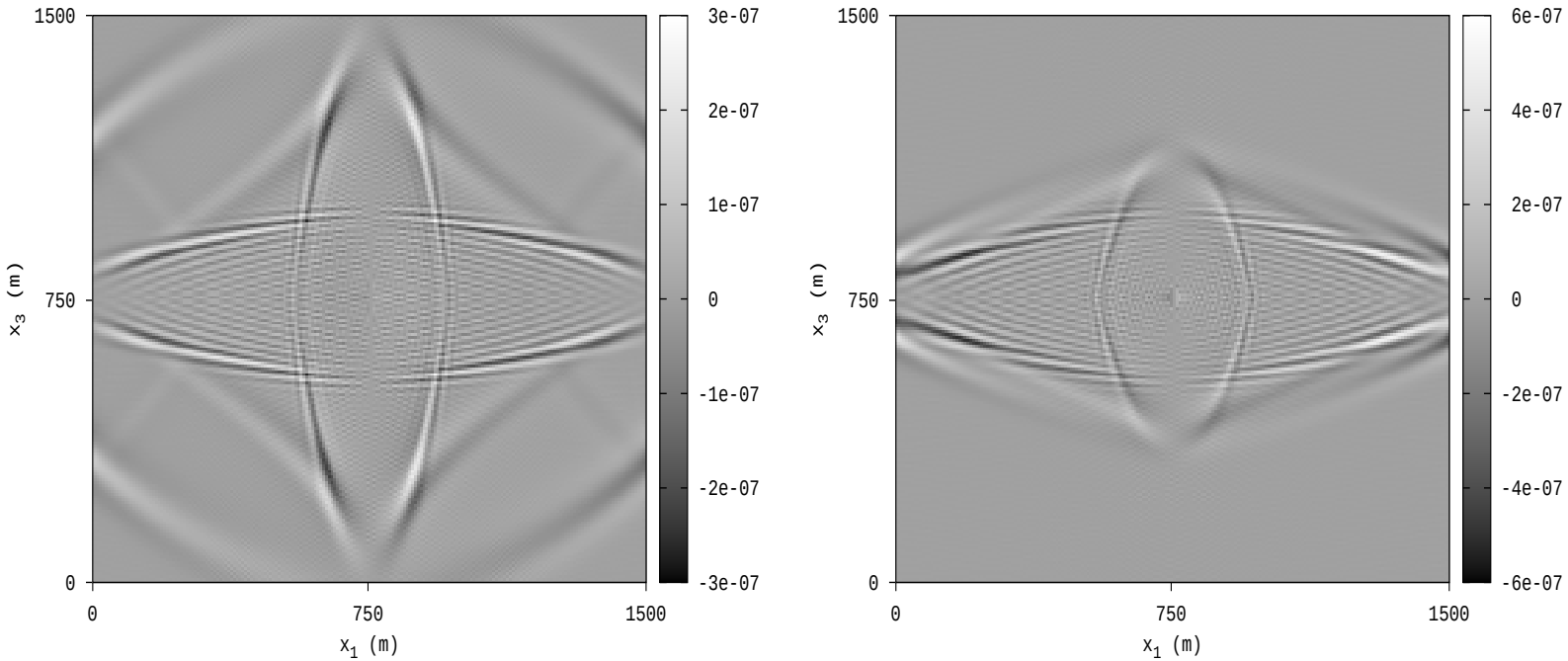

(a) : (b)

Figure 55 (a) : Brine saturation, Figure 55(b) : Patchy gas-brine saturation, gas saturation is 50%. Horizontal qSV wavefronts in Figure 55 b) travel at approximately the same speed than in Figure 55 a) and in Figure 52 b) for 10% patchy saturation. On the other hand the vertical qSV wavefronts in Figure 55 b) move slower than those in Figure 53 b) and exhibit triplication cusps close to the vertical direction.

3D VTI wave fronts at 200 ms, patchy gas-brine saturation.

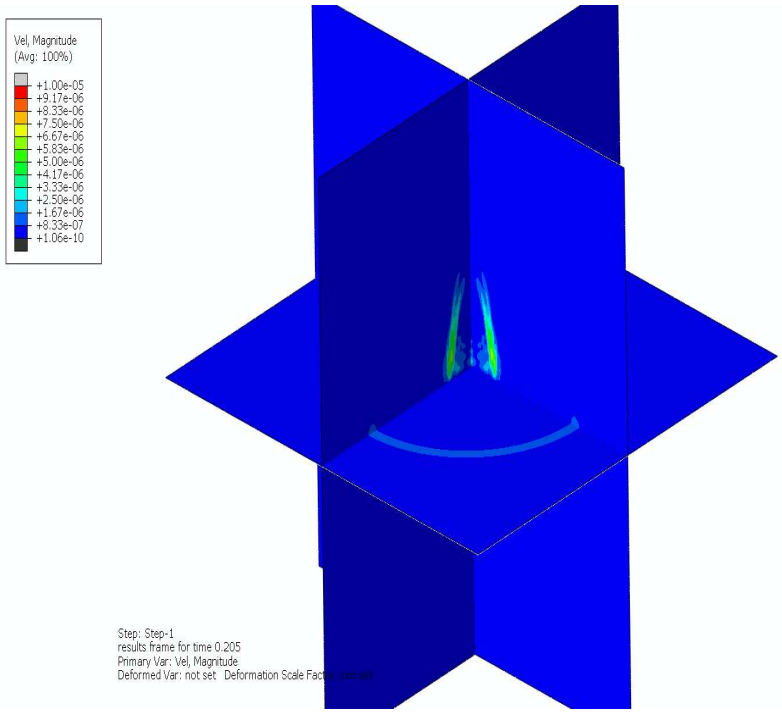

(a)

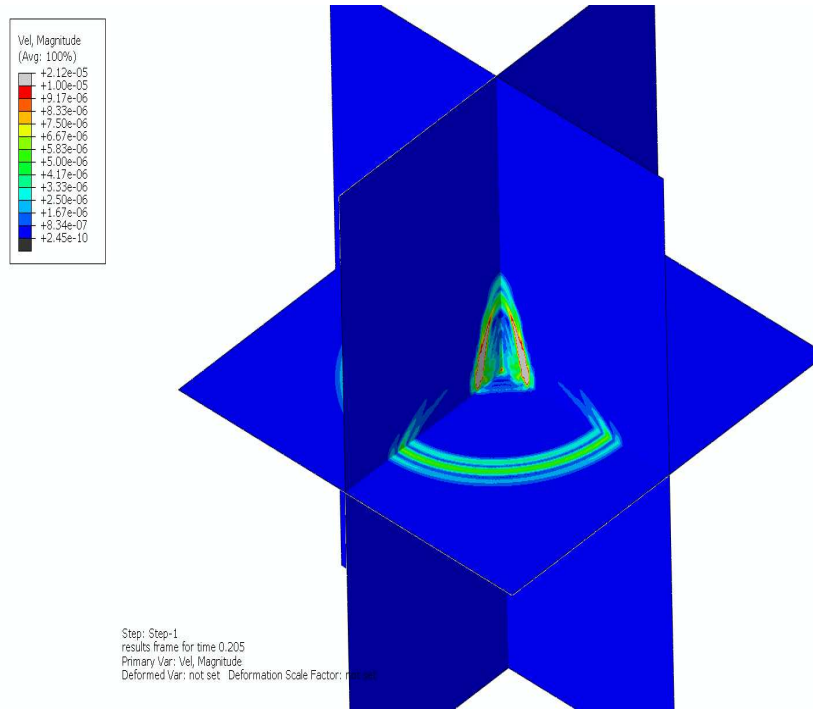

(b)

Figure 56 (a) 10% Overall gas saturation , Figure 56 (b) : Overall 50% gas saturation. Notice the higher attenuation in all wavefronts for 10% gas saturation in Figure 56 (a) saturation as compared with the case 50% case in Figure 56 (b), in accordance with the energy velocities Figure 34 b). The qP wavefront observed in Figure 48 for full brine saturation is not seen because this wavefront is traveling normally to the fracture layering, which is the direction of higher attenuation for these waves as indicated in Figure 34 a). Besides, qSV wavefronts are much less attenuated than qP waves since particles in qSV wavefronts move parallel to the fracture layering and suffer little attenuation in that direction according to Figure 34 b).

Snapshots of x-component of HTI wave fronts in the (x, y)-plane. Source is a shear strain in the (x, y)-plane. Full brine saturation

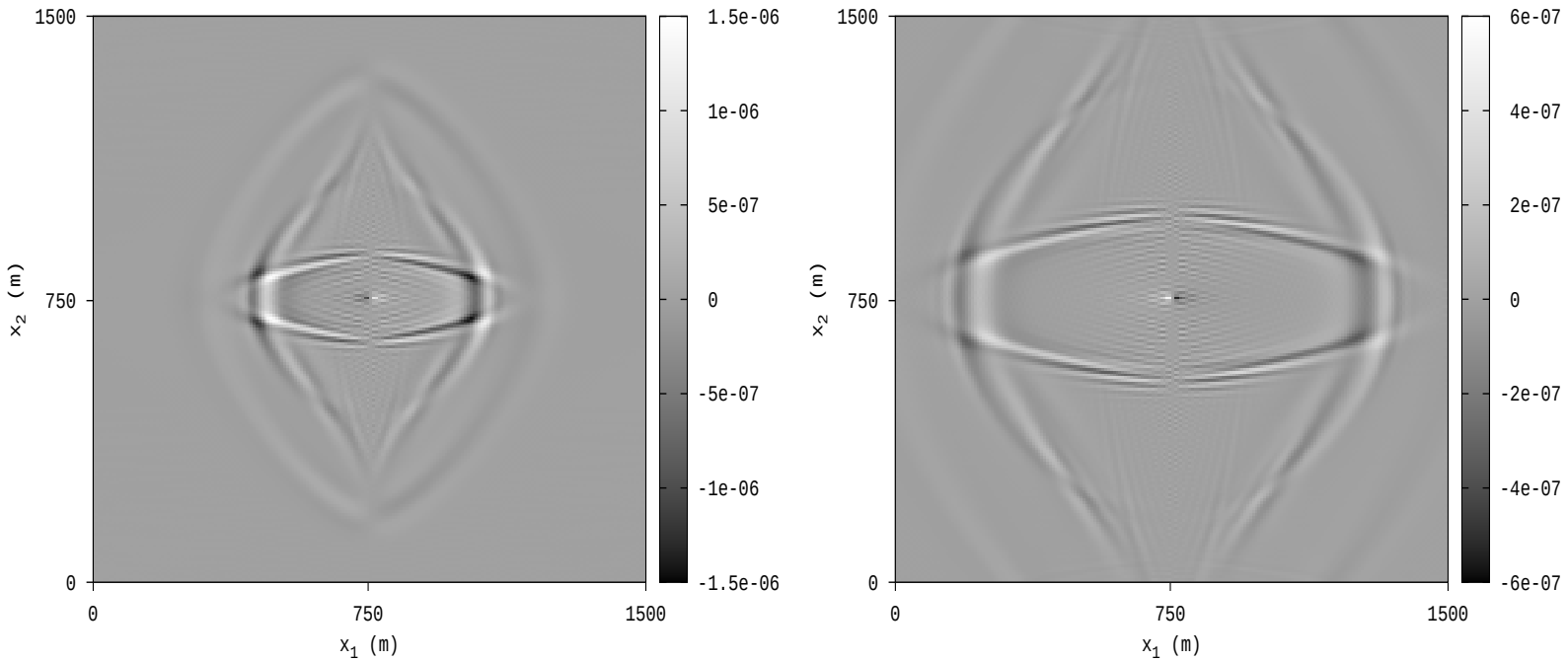

(a) (b)

(a) : x-component at 200 ms , (b) :x-component at 300 ms.

The fast wave front corresponds to the qP wave. Also can be seen two orthogonal wavefronts, an SH wavefront moving normally to the fracture layering plane and a qSV wavefront traveling parallel to the fracture layering. Also, qSV and SH wavefronts show approximately the same speed in the x-direction.

Snapshots of y-component of HTI wave fronts in the (x, y)-plane. Source is a shear strain in the (x, y)-plane. Full brine saturation

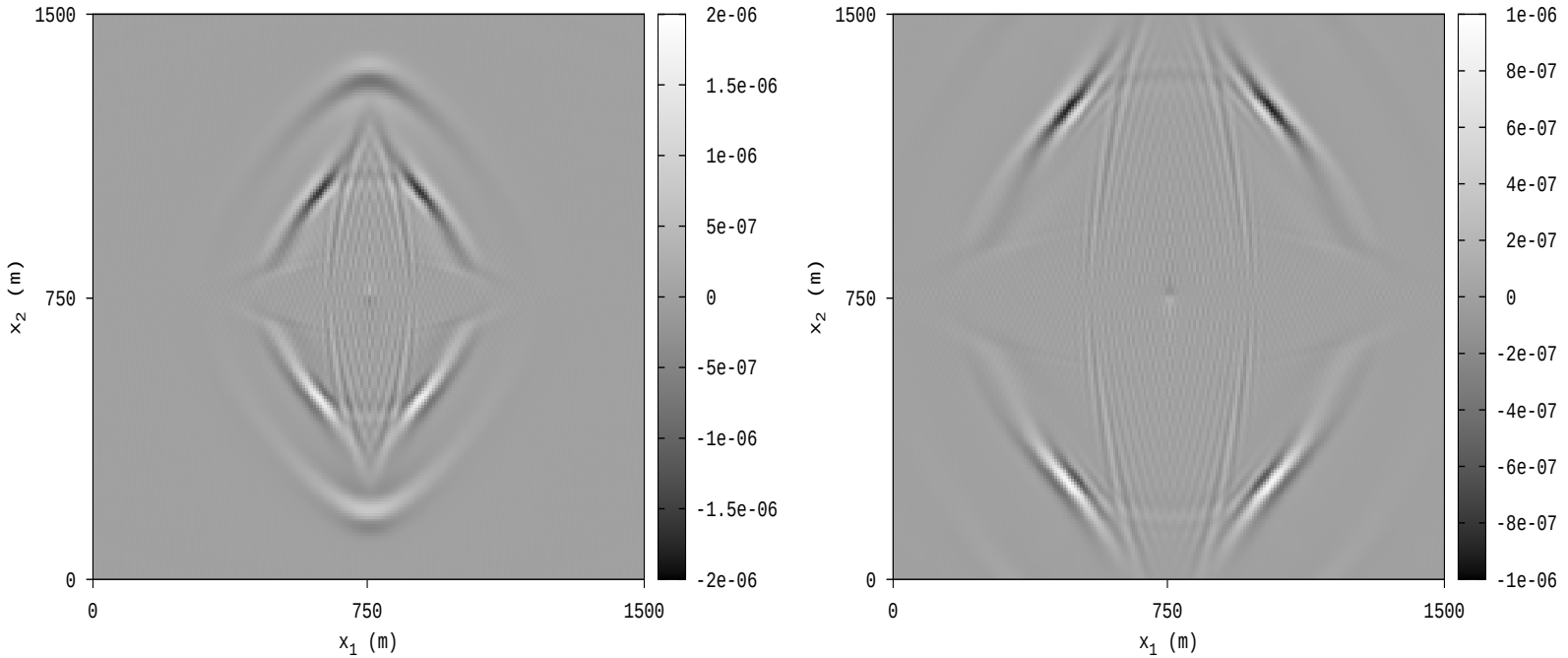

(a) (b)

(a) : y-component at 200 ms , (b) :y-component at 300 ms.

The fast wave front corresponds to the qP wave. Also can be seen two orthogonal wavefronts, an SH wavefront moving normally to the fracture layering plane and a qSV wavefront traveling parallel to the fracture layering. Also, qSV and SH wavefronts show approximately the same speed in the y-direction.

Snapshots of z-component of HTI wave fronts in the (x, y)-plane. Source is a shear strain in the (x, y)-plane. Full brine saturation.

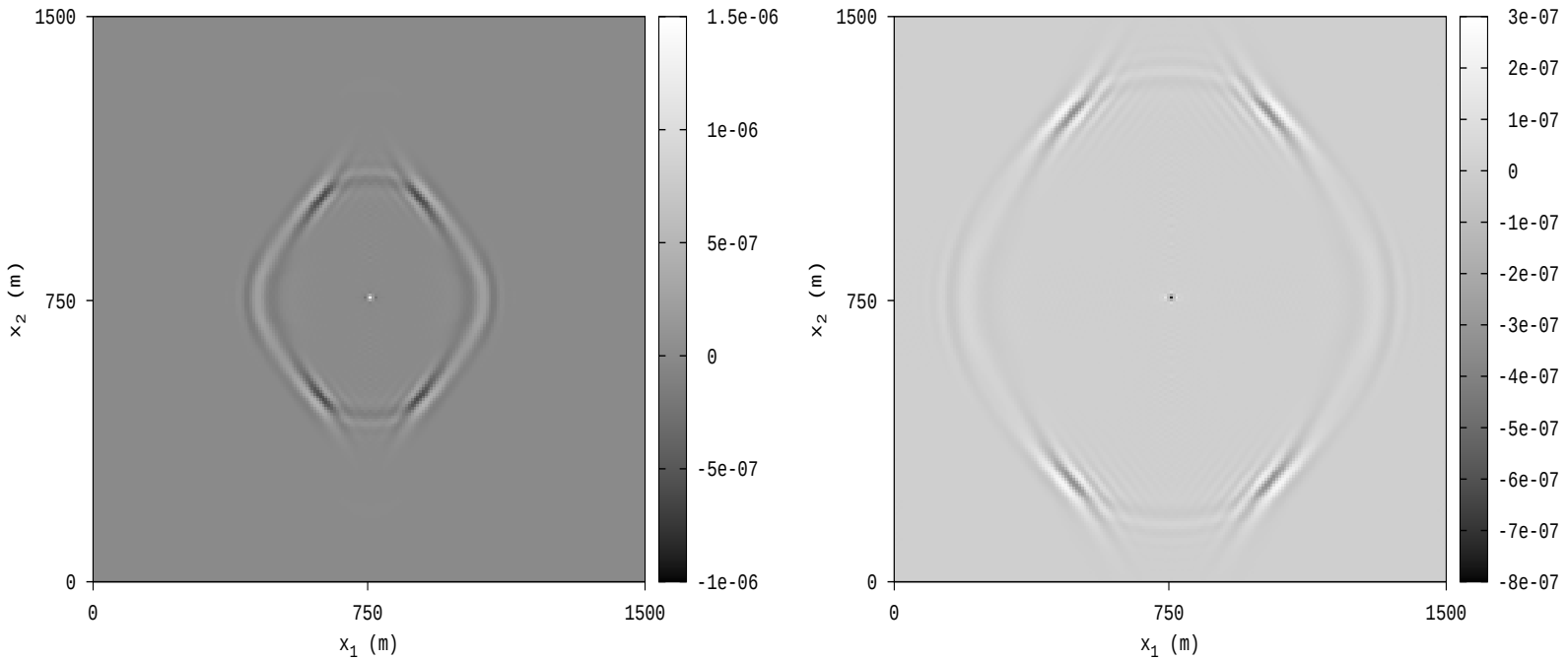

(a) (b)

(a) : z-component at 200 ms , (b) :z-component at 300 ms.
There is no qP wavefront because the shear source it is in the (x, y)-plane. Also can be seen SH and qSV wavefronts moving at approximately the same speed in the horizontal direction.

Snapshots of x-component of HTI wave fronts in the (x, z)-plane. Source is a shear strain in the (x, y)-plane. Full brine saturation

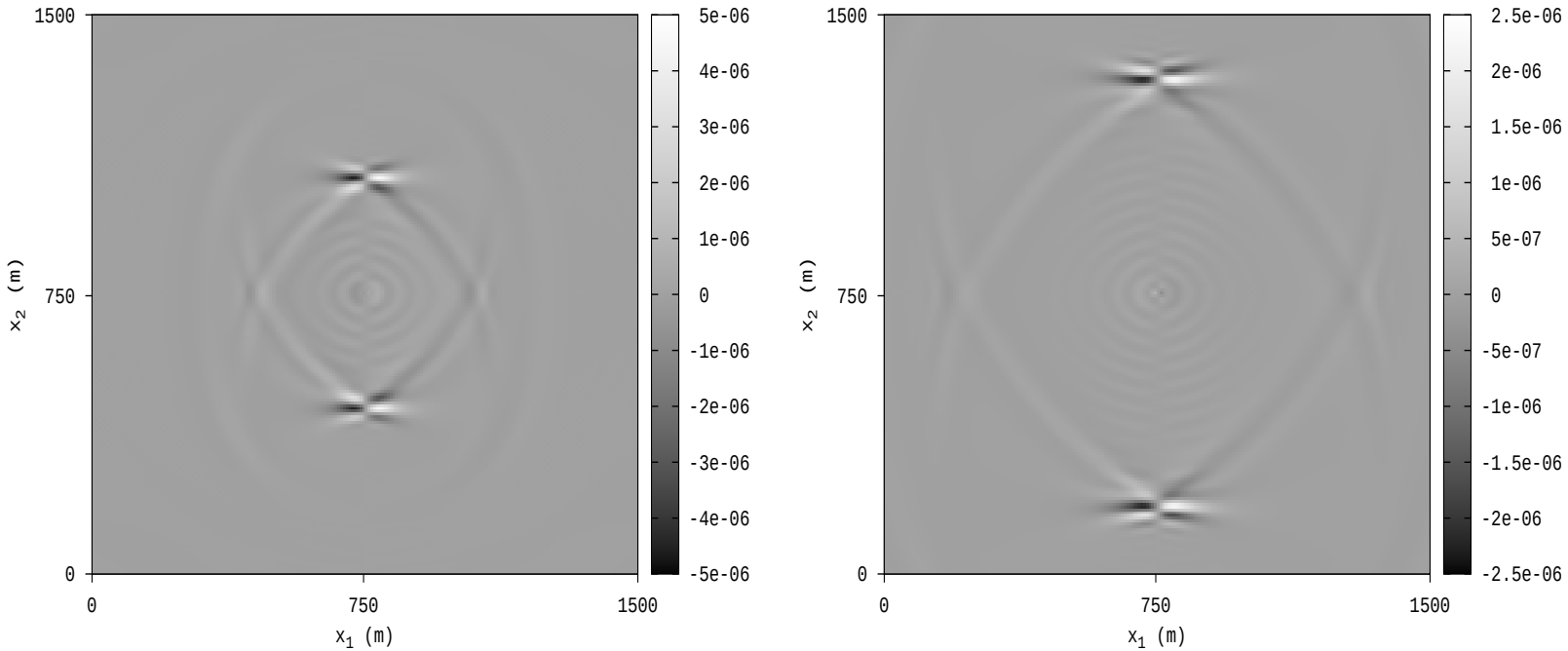

(a) (b)

(a) : x-component at 200 ms , (b) :x-component at 300 ms.
Se los dejo a los interpretes..., si no se entiende, se sacan..

Snapshots of y-component of HTI wave fronts in the (x, z)-plane. Source is a shear strain in the (x, y)-plane. Full brine saturation

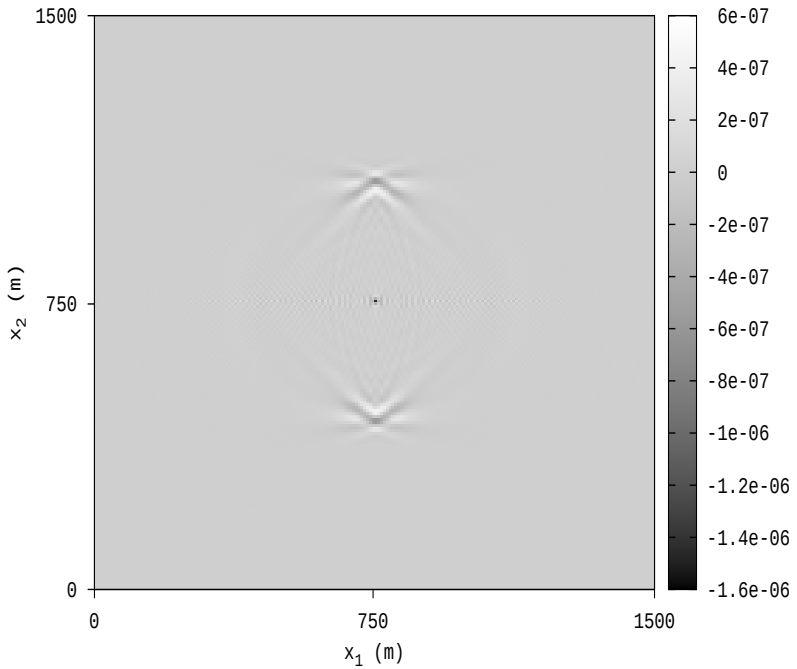

(a)

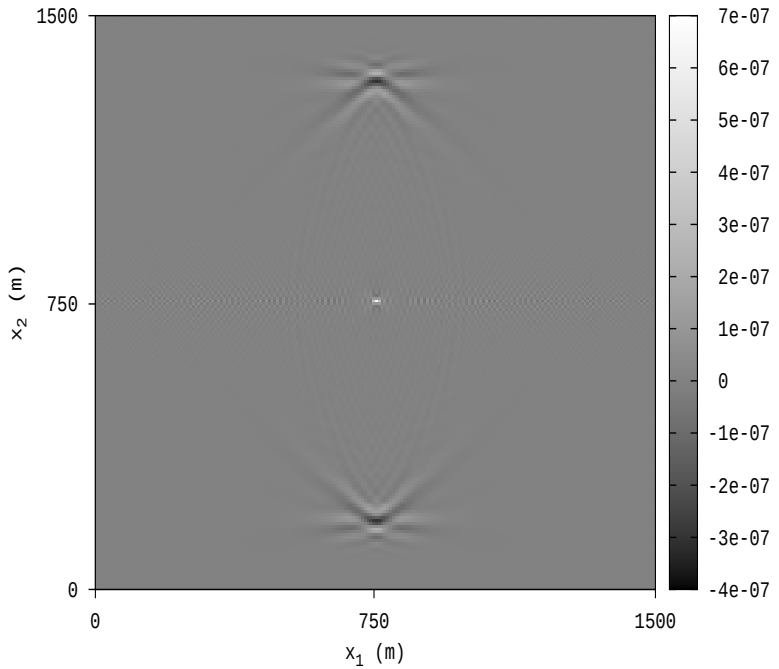

(b)

(a) : y-component at 200 ms , (b) :y-component at 300 ms.

Se los dejo a los interpretes...si no se entiende, se sacan..

Snapshots of z-component of HTI wave fronts in the (x, z)-plane. Source is a shear strain in the (x, y)-plane. Full brine saturation

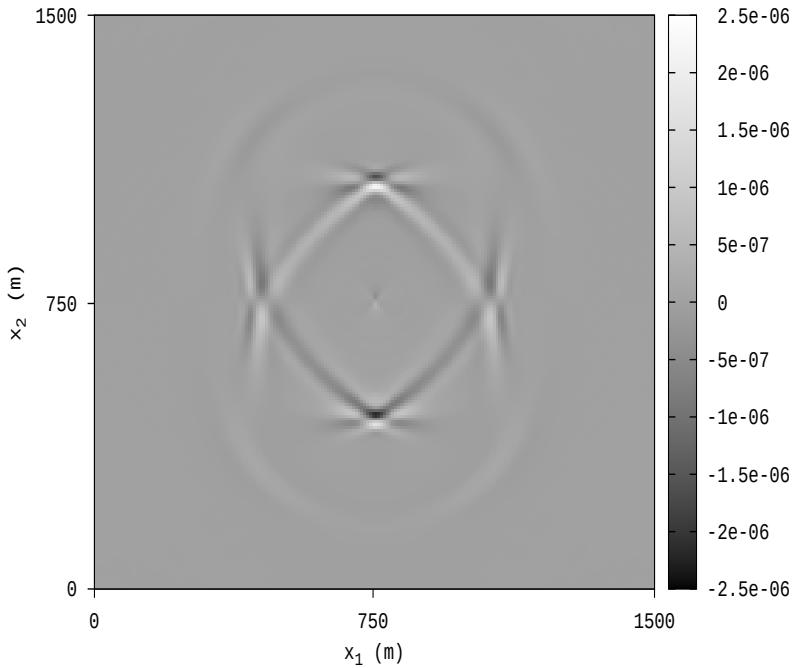

(a)

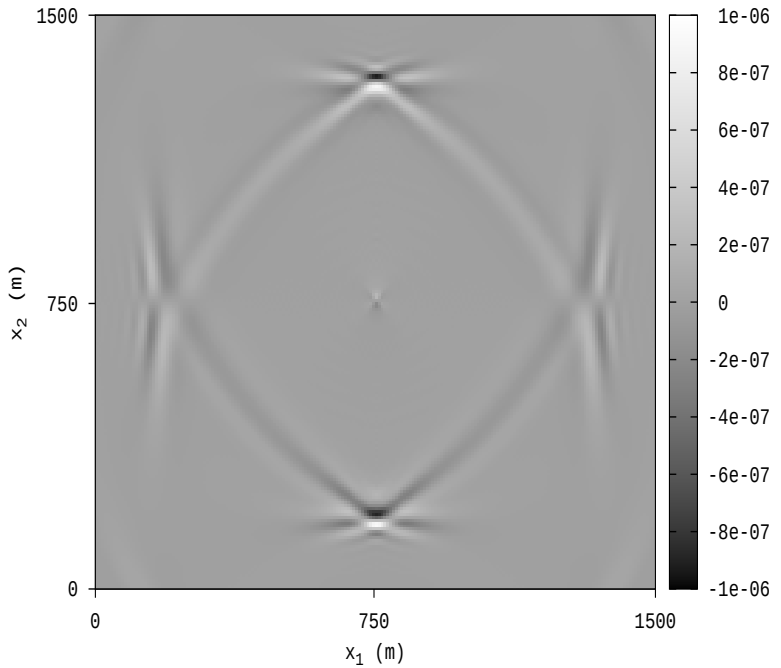

(b)

(a) : z-component at 200 ms , (b) :z-component at 300 ms.
Se los dejo a los interpretes...si no se entiende, se sacan..